

# Limits on Anomalous $WW\gamma$ and $WWZ$ Couplings from $WW/WZ \rightarrow e\nu jj$ Production

B. Abbott,<sup>47</sup> M. Abolins,<sup>44</sup> V. Abramov,<sup>19</sup> B.S. Acharya,<sup>13</sup> D.L. Adams,<sup>54</sup> M. Adams,<sup>30</sup> S. Ahn,<sup>29</sup> V. Akimov,<sup>17</sup> G.A. Alves,<sup>2</sup> N. Amos,<sup>43</sup> E.W. Anderson,<sup>36</sup> M.M. Baarmand,<sup>49</sup> V.V. Babintsev,<sup>19</sup> L. Babukhadia,<sup>49</sup> A. Baden,<sup>40</sup> B. Baldin,<sup>29</sup> S. Banerjee,<sup>13</sup> J. Bantly,<sup>53</sup> E. Barberis,<sup>22</sup> P. Baringer,<sup>37</sup> J.F. Bartlett,<sup>29</sup> U. Bassler,<sup>9</sup> A. Belyaev,<sup>18</sup> S.B. Beri,<sup>11</sup> G. Bernardi,<sup>9</sup> I. Bertram,<sup>20</sup> V.A. Bezzubov,<sup>19</sup> P.C. Bhat,<sup>29</sup> V. Bhatnagar,<sup>11</sup> M. Bhattacharjee,<sup>49</sup> G. Blazey,<sup>31</sup> S. Blessing,<sup>27</sup> A. Boehlein,<sup>29</sup> N.I. Bojko,<sup>19</sup> F. Borcherding,<sup>29</sup> A. Brandt,<sup>54</sup> R. Breedon,<sup>23</sup> G. Briskin,<sup>53</sup> R. Brock,<sup>44</sup> G. Brooijmans,<sup>29</sup> A. Bross,<sup>29</sup> D. Buchholz,<sup>32</sup> V. Buescher,<sup>48</sup> V.S. Burtovoi,<sup>19</sup> J.M. Butler,<sup>41</sup> W. Carvalho,<sup>3</sup> D. Casey,<sup>44</sup> Z. Casilum,<sup>49</sup> H. Castilla-Valdez,<sup>15</sup> D. Chakraborty,<sup>49</sup> K.M. Chan,<sup>48</sup> S.V. Chekulaev,<sup>19</sup> L.-P. Chen,<sup>22</sup> W. Chen,<sup>49</sup> D.K. Cho,<sup>48</sup> S. Choi,<sup>26</sup> S. Chopra,<sup>27</sup> B.C. Choudhary,<sup>26</sup> J.H. Christenson,<sup>29</sup> M. Chung,<sup>30</sup> D. Claes,<sup>45</sup> A.R. Clark,<sup>22</sup> W.G. Cobau,<sup>40</sup> J. Cochran,<sup>26</sup> L. Coney,<sup>34</sup> B. Connolly,<sup>27</sup> W.E. Cooper,<sup>29</sup> D. Coppage,<sup>37</sup> D. Cullen-Vidal,<sup>53</sup> M.A.C. Cummings,<sup>31</sup> D. Cutts,<sup>53</sup> O.I. Dahl,<sup>22</sup> K. Davis,<sup>21</sup> K. De,<sup>54</sup> K. Del Signore,<sup>43</sup> M. Demarteau,<sup>29</sup> D. Denisov,<sup>29</sup> S.P. Denisov,<sup>19</sup> H.T. Diehl,<sup>29</sup> M. Diesburg,<sup>29</sup> G. Di Loreto,<sup>44</sup> P. Draper,<sup>54</sup> Y. Ducros,<sup>10</sup> L.V. Dudko,<sup>18</sup> S.R. Dugad,<sup>13</sup> A. Dyshkant,<sup>19</sup> D. Edmunds,<sup>44</sup> J. Ellison,<sup>26</sup> V.D. Elvira,<sup>49</sup> R. Engelmann,<sup>49</sup> S. Eno,<sup>40</sup> G. Eppley,<sup>56</sup> P. Ermolov,<sup>18</sup> O.V. Eroshin,<sup>19</sup> J. Estrada,<sup>48</sup> H. Evans,<sup>46</sup> V.N. Evdokimov,<sup>19</sup> T. Fahland,<sup>25</sup> S. Feher,<sup>29</sup> D. Fein,<sup>21</sup> T. Ferbel,<sup>48</sup> H.E. Fisk,<sup>29</sup> Y. Fisyak,<sup>50</sup> E. Flattum,<sup>29</sup> F. Fleuret,<sup>22</sup> M. Fortner,<sup>31</sup> K.C. Frame,<sup>44</sup> S. Fuess,<sup>29</sup> E. Gallas,<sup>29</sup> A.N. Galyaev,<sup>19</sup> P. Gartung,<sup>26</sup> V. Gavrilov,<sup>17</sup> R.J. Genik II,<sup>20</sup> K. Genser,<sup>29</sup> C.E. Gerber,<sup>29</sup> Y. Gershtein,<sup>53</sup> B. Gibbard,<sup>50</sup> R. Gilmartin,<sup>27</sup> G. Ginther,<sup>48</sup> B. Gobbi,<sup>32</sup> B. Gómez,<sup>5</sup> G. Gómez,<sup>40</sup> P.I. Goncharov,<sup>19</sup> J.L. González Solís,<sup>15</sup> H. Gordon,<sup>50</sup> L.T. Goss,<sup>55</sup> K. Gounder,<sup>26</sup> A. Goussiou,<sup>49</sup> N. Graf,<sup>50</sup> P.D. Grannis,<sup>49</sup> D.R. Green,<sup>29</sup> J.A. Green,<sup>36</sup> H. Greenlee,<sup>29</sup> S. Grinstein,<sup>1</sup> P. Grudberg,<sup>22</sup> S. Grünendahl,<sup>29</sup> G. Guglielmo,<sup>52</sup> A. Gupta,<sup>13</sup> S.N. Gurzhiev,<sup>19</sup> G. Gutierrez,<sup>29</sup> P. Gutierrez,<sup>52</sup> N.J. Hadley,<sup>40</sup> H. Haggerty,<sup>29</sup> S. Hagopian,<sup>27</sup> V. Hagopian,<sup>27</sup> K.S. Hahn,<sup>48</sup> R.E. Hall,<sup>24</sup> P. Hanlet,<sup>42</sup> S. Hansen,<sup>29</sup> J.M. Hauptman,<sup>36</sup> C. Hays,<sup>46</sup> C. Hebert,<sup>37</sup> D. Hedin,<sup>31</sup> A.P. Heinson,<sup>26</sup> U. Heintz,<sup>41</sup> T. Heuring,<sup>27</sup> R. Hirosky,<sup>30</sup> J.D. Hobbs,<sup>49</sup> B. Hoeneisen,<sup>6</sup> J.S. Hoftun,<sup>53</sup> F. Hsieh,<sup>43</sup> A.S. Ito,<sup>29</sup> S.A. Jerger,<sup>44</sup> R. Jesik,<sup>33</sup> T. Joffe-Minor,<sup>32</sup> K. Johns,<sup>21</sup> M. Johnson,<sup>29</sup> A. Jonckheere,<sup>29</sup> M. Jones,<sup>28</sup> H. Jöstlein,<sup>29</sup> S.Y. Jun,<sup>32</sup> S. Kahn,<sup>50</sup> E. Kajfasz,<sup>8</sup> D. Karmanov,<sup>18</sup> D. Karmgard,<sup>34</sup> R. Kehoe,<sup>34</sup> S.K. Kim,<sup>14</sup> B. Klima,<sup>29</sup> C. Klopfenstein,<sup>23</sup> B. Knuteson,<sup>22</sup> W. Ko,<sup>23</sup> J.M. Kohli,<sup>11</sup> D. Koltick,<sup>35</sup> A.V. Kostritskiy,<sup>19</sup> J. Kotcher,<sup>50</sup> A.V. Kotwal,<sup>46</sup> A.V. Kozelov,<sup>19</sup> E.A. Kozlovsky,<sup>19</sup> J. Krane,<sup>36</sup> M.R. Krishnaswamy,<sup>13</sup> S. Krzywdzinski,<sup>29</sup> M. Kubantsev,<sup>38</sup> S. Kuleshov,<sup>17</sup> Y. Kulik,<sup>49</sup> S. Kunori,<sup>40</sup> G. Landsberg,<sup>53</sup> A. Leflat,<sup>18</sup> F. Lehner,<sup>29</sup> J. Li,<sup>54</sup> Q.Z. Li,<sup>29</sup> J.G.R. Lima,<sup>3</sup> D. Lincoln,<sup>29</sup> S.L. Linn,<sup>27</sup> J. Linnemann,<sup>44</sup> R. Lipton,<sup>29</sup> J.G. Lu,<sup>4</sup> A. Lucotte,<sup>49</sup> L. Lueking,<sup>29</sup> C. Lundstedt,<sup>45</sup> A.K.A. Maciel,<sup>31</sup> R.J. Madaras,<sup>22</sup> V. Manankov,<sup>18</sup> S. Mani,<sup>23</sup> H.S. Mao,<sup>4</sup> R. Markeloff,<sup>31</sup> T. Marshall,<sup>33</sup> M.I. Martin,<sup>29</sup> R.D. Martin,<sup>30</sup> K.M. Mauritz,<sup>36</sup> B. May,<sup>32</sup> A.A. Mayorov,<sup>33</sup> R. McCarthy,<sup>49</sup> J. McDonald,<sup>27</sup> T. McKibben,<sup>30</sup> T. McMahon,<sup>51</sup> H.L. Melanson,<sup>29</sup> M. Merkin,<sup>18</sup> K.W. Merritt,<sup>29</sup> C. Miao,<sup>53</sup> H. Miettinen,<sup>56</sup> A. Mincer,<sup>47</sup>

C.S. Mishra,<sup>29</sup> N. Mokhov,<sup>29</sup> N.K. Mondal,<sup>13</sup> H.E. Montgomery,<sup>29</sup> M. Mostafa,<sup>1</sup>  
 H. da Motta,<sup>2</sup> E. Nagy,<sup>8</sup> F. Nang,<sup>21</sup> M. Narain,<sup>41</sup> V.S. Narasimham,<sup>13</sup> H.A. Neal,<sup>43</sup>  
 J.P. Negret,<sup>5</sup> S. Negroni,<sup>8</sup> D. Norman,<sup>55</sup> L. Oesch,<sup>43</sup> V. Oguri,<sup>3</sup> B. Olivier,<sup>9</sup> N. Oshima,<sup>29</sup>  
 D. Owen,<sup>44</sup> P. Padley,<sup>56</sup> A. Para,<sup>29</sup> N. Parashar,<sup>42</sup> R. Partridge,<sup>53</sup> N. Parua,<sup>7</sup> M. Paterno,<sup>48</sup>  
     A. Patwa,<sup>49</sup> B. Pawlik,<sup>16</sup> J. Perkins,<sup>54</sup> M. Peters,<sup>28</sup> R. Piegaia,<sup>1</sup> H. Piekarcz,<sup>27</sup>  
 Y. Pischalnikov,<sup>35</sup> B.G. Pope,<sup>44</sup> E. Popkov,<sup>34</sup> H.B. Prosper,<sup>27</sup> S. Protopopescu,<sup>50</sup> J. Qian,<sup>43</sup>  
 P.Z. Quintas,<sup>29</sup> R. Raja,<sup>29</sup> S. Rajagopalan,<sup>50</sup> N.W. Reay,<sup>38</sup> S. Reucroft,<sup>42</sup> M. Rijssenbeek,<sup>49</sup>  
     T. Rockwell,<sup>44</sup> M. Roco,<sup>29</sup> P. Rubinov,<sup>32</sup> R. Ruchti,<sup>34</sup> J. Rutherford,<sup>21</sup> A. Santoro,<sup>2</sup>  
 L. Sawyer,<sup>39</sup> R.D. Schamberger,<sup>49</sup> H. Schellman,<sup>32</sup> A. Schwartzman,<sup>1</sup> J. Sculli,<sup>47</sup> N. Sen,<sup>56</sup>  
     E. Shabalina,<sup>18</sup> H.C. Shankar,<sup>13</sup> R.K. Shrivpuri,<sup>12</sup> D. Shpakov,<sup>49</sup> M. Shupe,<sup>21</sup>  
 R.A. Sidwell,<sup>38</sup> H. Singh,<sup>26</sup> J.B. Singh,<sup>11</sup> V. Sirotenko,<sup>31</sup> P. Slattery,<sup>48</sup> E. Smith,<sup>52</sup>  
 R.P. Smith,<sup>29</sup> R. Snihur,<sup>32</sup> G.R. Snow,<sup>45</sup> J. Snow,<sup>51</sup> S. Snyder,<sup>50</sup> J. Solomon,<sup>30</sup> X.F. Song,<sup>4</sup>  
     V. Sorín,<sup>1</sup> M. Sosebee,<sup>54</sup> N. Sotnikova,<sup>18</sup> M. Souza,<sup>2</sup> N.R. Stanton,<sup>38</sup> G. Steinbrück,<sup>46</sup>  
     R.W. Stephens,<sup>54</sup> M.L. Stevenson,<sup>22</sup> F. Stichelbaut,<sup>50</sup> D. Stoker,<sup>25</sup> V. Stolin,<sup>17</sup>  
 D.A. Stoyanova,<sup>19</sup> M. Strauss,<sup>52</sup> K. Streets,<sup>47</sup> M. Strovink,<sup>22</sup> L. Stutte,<sup>29</sup> A. Sznajder,<sup>3</sup>  
 J. Tarazi,<sup>25</sup> M. Tartaglia,<sup>29</sup> T.L.T. Thomas,<sup>32</sup> J. Thompson,<sup>40</sup> D. Toback,<sup>40</sup> T.G. Tripp,<sup>22</sup>  
 A.S. Turcot,<sup>43</sup> P.M. Tuts,<sup>46</sup> P. van Gemmeren,<sup>29</sup> V. Vaniev,<sup>19</sup> N. Varelas,<sup>30</sup> A.A. Volkov,<sup>19</sup>  
     A.P. Vorobiev,<sup>19</sup> H.D. Wahl,<sup>27</sup> J. Warchol,<sup>34</sup> G. Watts,<sup>57</sup> M. Wayne,<sup>34</sup> H. Weerts,<sup>44</sup>  
     A. White,<sup>54</sup> J.T. White,<sup>55</sup> J.A. Wightman,<sup>36</sup> S. Willis,<sup>31</sup> S.J. Wimpenny,<sup>26</sup>  
 J.V.D. Wirjawan,<sup>55</sup> J. Womersley,<sup>29</sup> D.R. Wood,<sup>42</sup> R. Yamada,<sup>29</sup> P. Yamin,<sup>50</sup> T. Yasuda,<sup>29</sup>  
 K. Yip,<sup>29</sup> S. Youssef,<sup>27</sup> J. Yu,<sup>29</sup> Y. Yu,<sup>14</sup> M. Zanabria,<sup>5</sup> H. Zheng,<sup>34</sup> Z. Zhou,<sup>36</sup> Z.H. Zhu,<sup>48</sup>  
     M. Zielinski,<sup>48</sup> D. Ziemińska,<sup>33</sup> A. Ziemiński,<sup>33</sup> V. Zutshi,<sup>48</sup> E.G. Zverev,<sup>18</sup>  
     and A. Zylberstejn<sup>10</sup>  
     (DØ Collaboration)

<sup>1</sup> *Universidad de Buenos Aires, Buenos Aires, Argentina*

<sup>2</sup> *LAFEX, Centro Brasileiro de Pesquisas Físicas, Rio de Janeiro, Brazil*

<sup>3</sup> *Universidade do Estado do Rio de Janeiro, Rio de Janeiro, Brazil*

<sup>4</sup> *Institute of High Energy Physics, Beijing, People's Republic of China*

<sup>5</sup> *Universidad de los Andes, Bogotá, Colombia*

<sup>6</sup> *Universidad San Francisco de Quito, Quito, Ecuador*

<sup>7</sup> *Institut des Sciences Nucléaires, IN2P3-CNRS, Université de Grenoble 1, Grenoble, France*

<sup>8</sup> *Centre de Physique des Particules de Marseille, IN2P3-CNRS, Marseille, France*

<sup>9</sup> *LPNHE, Universités Paris VI and VII, IN2P3-CNRS, Paris, France*

<sup>10</sup> *DAPNIA/Service de Physique des Particules, CEA, Saclay, France*

<sup>11</sup> *Panjab University, Chandigarh, India*

<sup>12</sup> *Delhi University, Delhi, India*

<sup>13</sup> *Tata Institute of Fundamental Research, Mumbai, India*

<sup>14</sup> *Seoul National University, Seoul, Korea*

<sup>15</sup> *CINVESTAV, Mexico City, Mexico*

<sup>16</sup> *Institute of Nuclear Physics, Kraków, Poland*

<sup>17</sup> *Institute for Theoretical and Experimental Physics, Moscow, Russia*

<sup>18</sup> *Moscow State University, Moscow, Russia*

<sup>19</sup> *Institute for High Energy Physics, Protvino, Russia*

<sup>20</sup> *Lancaster University, Lancaster, United Kingdom*

<sup>21</sup>*University of Arizona, Tucson, Arizona 85721*

<sup>22</sup>*Lawrence Berkeley National Laboratory and University of California, Berkeley, California 94720*

<sup>23</sup>*University of California, Davis, California 95616*

<sup>24</sup>*California State University, Fresno, California 93740*

<sup>25</sup>*University of California, Irvine, California 92697*

<sup>26</sup>*University of California, Riverside, California 92521*

<sup>27</sup>*Florida State University, Tallahassee, Florida 32306*

<sup>28</sup>*University of Hawaii, Honolulu, Hawaii 96822*

<sup>29</sup>*Fermi National Accelerator Laboratory, Batavia, Illinois 60510*

<sup>30</sup>*University of Illinois at Chicago, Chicago, Illinois 60607*

<sup>31</sup>*Northern Illinois University, DeKalb, Illinois 60115*

<sup>32</sup>*Northwestern University, Evanston, Illinois 60208*

<sup>33</sup>*Indiana University, Bloomington, Indiana 47405*

<sup>34</sup>*University of Notre Dame, Notre Dame, Indiana 46556*

<sup>35</sup>*Purdue University, West Lafayette, Indiana 47907*

<sup>36</sup>*Iowa State University, Ames, Iowa 50011*

<sup>37</sup>*University of Kansas, Lawrence, Kansas 66045*

<sup>38</sup>*Kansas State University, Manhattan, Kansas 66506*

<sup>39</sup>*Louisiana Tech University, Ruston, Louisiana 71272*

<sup>40</sup>*University of Maryland, College Park, Maryland 20742*

<sup>41</sup>*Boston University, Boston, Massachusetts 02215*

<sup>42</sup>*Northeastern University, Boston, Massachusetts 02115*

<sup>43</sup>*University of Michigan, Ann Arbor, Michigan 48109*

<sup>44</sup>*Michigan State University, East Lansing, Michigan 48824*

<sup>45</sup>*University of Nebraska, Lincoln, Nebraska 68588*

<sup>46</sup>*Columbia University, New York, New York 10027*

<sup>47</sup>*New York University, New York, New York 10003*

<sup>48</sup>*University of Rochester, Rochester, New York 14627*

<sup>49</sup>*State University of New York, Stony Brook, New York 11794*

<sup>50</sup>*Brookhaven National Laboratory, Upton, New York 11973*

<sup>51</sup>*Langston University, Langston, Oklahoma 73050*

<sup>52</sup>*University of Oklahoma, Norman, Oklahoma 73019*

<sup>53</sup>*Brown University, Providence, Rhode Island 02912*

<sup>54</sup>*University of Texas, Arlington, Texas 76019*

<sup>55</sup>*Texas A&M University, College Station, Texas 77843*

<sup>56</sup>*Rice University, Houston, Texas 77005*

<sup>57</sup>*University of Washington, Seattle, Washington 98195*

## Abstract

Limits on anomalous  $WW\gamma$  and  $WWZ$  couplings are presented from a study of  $WW/WZ \rightarrow e\nu jj$  events in  $p\bar{p}$  collisions at  $\sqrt{s} = 1.8$  TeV using the data sample collected by the DØ detector during the 1993–1995 Tevatron collider

run at Fermilab. The results are combined with those of an earlier study using the data sample of the 1992–1993 run. A fit to the transverse momentum spectrum of the  $W$  boson yields direct limits on the anomalous  $WW\gamma$  and  $WWZ$  couplings. With the assumption that the  $WW\gamma$  and  $WWZ$  couplings are equal, we obtain  $-0.34 < \lambda < 0.36$  (with  $\Delta\kappa = 0$ ) and  $-0.43 < \Delta\kappa < 0.59$  (with  $\lambda = 0$ ) at the 95% confidence level for a form factor scale  $\Lambda = 2.0$  TeV.

## I. INTRODUCTION

The Tevatron  $p\bar{p}$  collider at Fermilab offers one of the best opportunities to test the trilinear gauge boson couplings [1–3], which are a direct consequence of the non-Abelian  $SU(2) \times U(1)$  gauge structure of the standard model (SM). The trilinear gauge boson couplings can be measured directly from the gauge boson pair (diboson) production processes. Production of  $WW$  and  $WZ$  boson pairs in  $p\bar{p}$  collisions at  $\sqrt{s} = 1.8$  TeV occurs as an  $s$ -channel boson exchange processes or a  $t$ - or  $u$ -channel quark exchange processes in the standard model, as shown in Fig. 1. There are substantial cancellations between the  $t$ - or  $u$ -diagrams, which involve only the couplings of the bosons to fermions, and the  $s$ -channel diagrams which contain the three-boson couplings. These cancellations are essential to make the SM diboson production processes unitary and renormalizable. Since the fermionic couplings of the  $W$ ,  $Z$ , and  $\gamma$  have been well tested [4], we may regard diboson production as primarily a test of the three-boson couplings. Production of  $WW$  pairs is sensitive to both  $WW\gamma$  and  $WWZ$  couplings;  $WZ$  production is sensitive only to the  $WWZ$  couplings.

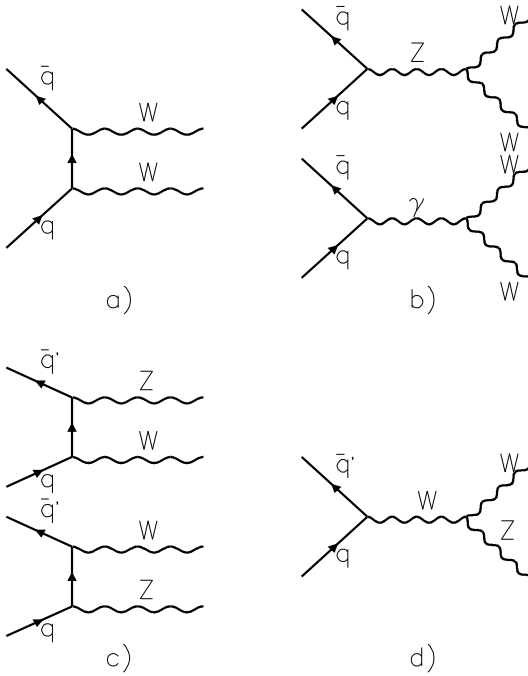


FIG. 1. Feynman diagrams for  $WW$  and  $WZ$  production at leading order. a) and c):  $t$ - and  $u$ -channel quark exchange diagrams; b) and d):  $s$ -channel diagrams with three-boson couplings.

A generalized effective Lagrangian has been developed to describe the trilinear gauge boson couplings [5]. The Lorentz-invariant effective Lagrangian for the gauge boson self-interactions contains fourteen dimensionless coupling parameters,  $\lambda_V$ ,  $\kappa_V$ ,  $g_1^V$ ,  $\tilde{\lambda}_V$ ,  $\tilde{\kappa}_V$ ,  $g_4^V$ , and  $g_5^V$  ( $V = Z$  or  $\gamma$ ), seven for  $WWZ$  interactions and another seven for  $WW\gamma$  interactions, and two overall couplings,  $g_{WW\gamma} = -e$  and  $g_{WWZ} = -e \cot \theta_W$ , where  $e$  and  $\theta_W$  are the positron charge and the weak mixing angle. The couplings  $\lambda_V$  and  $\kappa_V$  conserve charge  $C$  and parity  $P$ . The couplings  $g_4^V$  are odd under  $CP$  and  $C$ ,  $g_5^V$  are odd under  $C$  and  $P$ , and

$\tilde{\kappa}_V$  and  $\tilde{\lambda}_V$  are odd under  $CP$  and  $P$ . Within the SM at tree level, all of the couplings are zero except  $g_1^V$  and  $\kappa_V$  ( $g_1^V = g_1^Z = \kappa_\gamma = \kappa_Z = 1$ ). Electromagnetic gauge invariance does not allow deviations of  $g_1^V$ ,  $g_4^V$ , and  $g_5^V$  from their SM values of 1, 0, and 0, respectively, for on-shell photons. The  $CP$ -violating  $WW\gamma$  couplings  $\tilde{\lambda}_\gamma$  and  $\tilde{\kappa}_\gamma$  are tightly constrained by measurements of the neutron electric dipole moment [6]. In the present study, we assume  $C$ ,  $P$  and  $CP$  symmetries are conserved, reducing the number of coupling parameters to five:  $\kappa_\gamma$ ,  $\kappa_Z$ ,  $\lambda_\gamma$ ,  $\lambda_Z$  and  $g_1^Z$ .

For couplings with non-SM values, the cross sections for gauge boson pair production increase because the cancellation between the  $t$ - and  $u$ -channel diagrams and the  $s$ -channel diagrams is destroyed. This results in unphysically large cross sections at high energies, eventually violating tree-level unitarity. A consistent description therefore requires anomalous couplings to show a form factor behavior which causes them to vanish at very high energies. We will use dipole form factors, e.g.  $\lambda_V(\hat{s}) = \lambda_V/(1 + \hat{s}/\Lambda^2)^2$ , where  $\hat{s}$  is the square of the invariant mass of the gauge boson pair system. The anomalous coupling parameters are restricted by  $S$ -matrix unitarity for a given form factor scale  $\Lambda$ . Assuming that the independent coupling parameters are  $\kappa = \kappa_\gamma = \kappa_Z$  and  $\lambda = \lambda_\gamma = \lambda_Z$ , tree-level unitarity is satisfied if  $\Lambda \leq [6.88/((\kappa - 1)^2 + 2\lambda^2)]^{1/4}$  TeV [2,7]. The experimental limits on anomalous couplings are compared with the bounds derived from  $S$ -matrix unitarity. Experiments constrain the trilinear gauge boson couplings non-trivially only if the experimental limits are more stringent than the unitarity bounds for a given value of  $\Lambda$ .

The effect of anomalous values of  $\lambda_V$  on the helicity amplitudes is enhanced by  $\hat{s}$  in both the  $WW$  and  $WZ$  production processes. On the other hand, terms containing  $\Delta\kappa_V$  ( $= \kappa_V - 1$ ) grow with  $\sqrt{\hat{s}}$  in the  $WZ$  production process, and with  $\hat{s}$  in the  $WW$  production process. Limits on  $\Delta\kappa_V$  from the study of  $WW$  production are therefore expected to be tighter than those from the  $WZ$  production.

Since anomalous couplings only contribute via  $s$ -channel  $W$ ,  $Z$  or photon exchange, their effects are mainly in the region of small vector boson rapidities, and the transverse momentum distribution of the vector boson is particularly sensitive to anomalous trilinear gauge boson couplings. This is demonstrated in Fig. 2 which shows the distribution of the  $W$  boson transverse momentum  $p_T^W$  in simulated  $p\bar{p} \rightarrow WW + X \rightarrow e\nu jj + X$  events at the Tevatron for SM and for anomalous trilinear gauge boson couplings. A dipole form factor with a scale  $\Lambda = 1.5$  TeV is used and the couplings for  $WW\gamma$  and  $WWZ$  are assumed to be equal.

Trilinear gauge boson couplings can be measured by comparing the shapes of the  $p_T$  distributions of the final state gauge bosons to the theoretical prediction. Even if the background is much larger than the expected gauge boson pair production signal as in the  $WW/WZ \rightarrow e\nu jj$  process, limits on anomalous couplings can still be set using a kinematical region where the effects of anomalous trilinear gauge boson couplings dominate.

The trilinear gauge boson couplings have been studied by several experiments. The  $WW\gamma$  couplings have been studied using  $W\gamma$  production events in  $p\bar{p}$  collisions by the UA2 [8], CDF [9], and DØ [10,11] experiments. The UA2 results are based on data taken during the 1988–1990 CERN  $p\bar{p}$  collider run at  $\sqrt{s} = 630$  GeV with an integrated luminosity of  $13 \text{ pb}^{-1}$ . CDF and DØ have studied  $W\gamma$  production using the 1992–1993 and 1993–1995

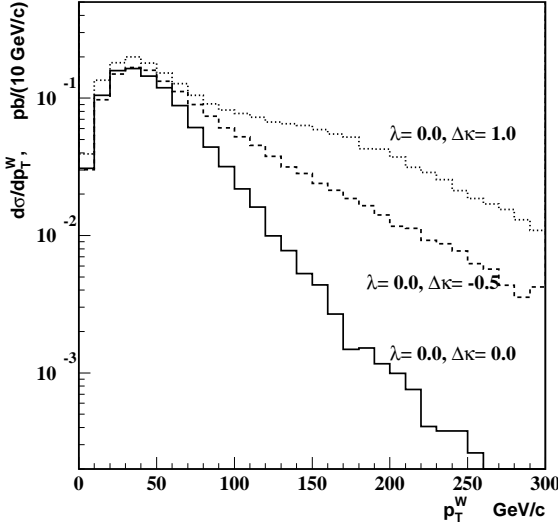


FIG. 2. The  $p_T^W$  spectrum of generated  $p\bar{p} \rightarrow WW \rightarrow e\nu jj$  events with SM couplings and two examples of anomalous couplings.

Fermilab  $p\bar{p}$  collider data at  $\sqrt{s} = 1.8$  TeV. The  $WWZ$  couplings together with the  $WW\gamma$  couplings have also been studied by the CDF and DØ collaborations using  $W$  boson pair production in the dilepton decay modes [11–13] and  $WW/WZ$  production in the single-lepton modes [11,14–16]. Experiments at the CERN LEP Collider have recently reported results from their measurements [17].

In this report, we present a detailed description of a previously summarized study [18] of  $WW$  or  $WZ$  production with a  $W$  boson decaying into an electron (or a positron) and an antineutrino (or a neutrino) and a second  $W$  boson or a  $Z$  boson decaying into two jets [19]. Due to the limited jet energy resolution of the detector, a hadronic decay of a  $W$  boson can not be differentiated from that of a  $Z$  boson. This analysis is based on the data collected during the 1993–1995 Tevatron collider run at Fermilab. From the observed candidate events and background estimates, 95% confidence level (C.L.) limits on the anomalous trilinear gauge boson couplings are set. The results are combined with those from the 1992–1993 data set to provide the final limits on the couplings from this analysis.

Brief summaries of the DØ detector and the multilevel trigger and data acquisition system are presented in Sections II and III. Sections IV, V and VI describe our particle identification methods, data sample, and event selection criteria. Sections VII and VIII are devoted to the detection efficiency and background estimates. The results and conclusions are presented in Sections IX and X.

## II. THE DØ DETECTOR

The DØ detector [20], illustrated in Fig. 3, is a general-purpose detector designed for the study of proton-antiproton collisions at  $\sqrt{s} = 1.8$  TeV and is located at the DØ interaction region of the Tevatron ring at Fermilab.

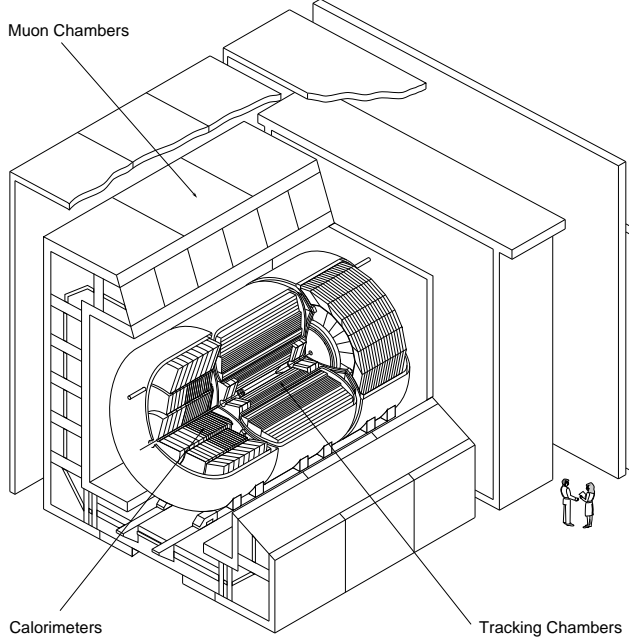


FIG. 3. Cutaway view of the DØ detector

The innermost part of the DØ detector is a set of tracking detectors surrounding the beam pipe. The DØ detector does not have a central magnetic field. The absence of a central magnetic field enables the calorimeters to be hermetic. To identify muons, an additional set of tracking chambers is located outside of the calorimeter. To provide a measurement of the muon momentum, magnetized iron toroids are placed between the first two muon tracking layers.

The full detector is about 13 m high  $\times$  11 m wide  $\times$  17 m long with a total weight of about 5500 tons. The Tevatron beam pipe passes through the center of the detector, while the Main Ring beam pipe passes through the upper portion of the calorimeter, approximately 2 m above the Tevatron beam pipe. The coordinate system used in DØ is a right-handed coordinate system, with the  $z$ -axis along the direction of the proton beam (southward) and the  $y$ -axis pointing up. Therefore the polar angle  $\theta = 0$  along the proton beam direction, and the azimuthal angle  $\phi = 0$  along the eastward direction. Instead of  $\theta$ , the pseudorapidity,  $\eta = -\ln[\tan(\theta/2)]$ , is often used. This quantity approximates the true rapidity  $y = 1/2 \ln[(E + p_z)/(E - p_z)]$ , when the rest mass is much smaller than the total energy.

### A. Tracking Detectors

The tracking chambers and transition radiation detector make up the central detector (CD). The main purpose of the CD is to measure the position of charged particle tracks and determine the  $z$  position of the interaction vertex. This information can be used to determine whether an electromagnetic energy cluster in the calorimeter is caused by an electron or by

a photon. Additional information such as the number of tracks and the ionization energy along the track ( $dE/dx$ ) can be used to determine whether the track is caused by several closely spaced charged particles, such as a photon conversion.

The CD consists of four separate subsystems: the vertex drift chamber (VTX), the transition radiation detector (TRD), the central drift chamber (CDC), and two forward drift chambers (FDC). The full set of CD detectors fits within the inner cylindrical aperture of the calorimeters in a volume of radius  $r = 78$  cm and length  $l = 270$  cm. The system provides charged-particle tracking over the region  $|\eta| < 3.2$ . It measures the trajectories of charged particles with a resolution of 2.5 mrad in  $\phi$  and 28 mrad in  $\theta$ . From these measurements the position of the interaction vertex along the beam direction ( $z$ ) can be determined with a resolution of 6 mm.

The VTX is the innermost tracking chamber in the D $\emptyset$  detector. It is made of three mechanically independent concentric layers of cells parallel to the beam pipe, from  $r = 3.7$  cm to 16.2 cm. The innermost layer has sixteen cells while the outer two layers have thirty-two cells each.

The TRD occupies the space between the VTX and the CDC; it extends from  $r = 17.5$  cm to 49 cm. The TRD consists of three separate units, each containing a radiator (393 foils of 18  $\mu\text{m}$  thick polypropylene in a volume filled with nitrogen gas) and an X-ray detection chamber filled with Xe gas. The TRD information is not used in this analysis.

The CDC is a cylindrical drift chamber of length 184 cm located between  $r = 49.5$  and  $r = 74.5$  cm, which provides coverage for  $|\eta| < 1.2$ . It is made up of four concentric rings of 32 azimuthal cells per ring. Each cell contains seven sense wires (staggered by 200  $\mu\text{m}$  relative to each other to help resolve left-right ambiguities), and two delay lines. The  $r\phi$  position of a hit is determined via the drift time and the wire hit. The  $z$  position of a hit is measured using inductive delay lines embedded in the module walls in the sense wire plane.

The FDC consists of two sets of drift chambers located at the ends of the CDC. They perform the same function as the CDC for  $1.4 < |\eta| < 3.1$ . Each FDC package consists of three separate chambers: a  $\Phi$  module, whose sense wires are radial and measure the  $\phi$  coordinate, sandwiched between a pair of  $\Theta$  modules whose sense wires measure the  $\theta$  coordinate.

## B. Calorimeters

The D $\emptyset$  calorimeter is a sampling calorimeter, with liquid argon as the ionization medium. The primary absorber material is depleted uranium, with copper and stainless steel in the outer regions. The calorimeter is divided into three modules contained in separate cryostats: the Central Calorimeter (CC), the North End Calorimeter (ECN), and the South End Calorimeter (ECS). The readout cells are arranged with a pseudo-projective geometry pointing to the interaction region.

The calorimeter modules are subdivided by depth into three distinct types of modules: an electromagnetic section (EM) with relatively thin uranium absorber plates, a fine-hadronic

section (FH) with thicker uranium plates, and a coarse-hadronic section (CH) with thick copper or stainless steel plates. There are four separate depth layers for the EM modules in both the CC and EC. The first two layers are 2 radiation lengths thick in the CC and 0.3 and 2.6 radiation lengths thick in the EC and measure the longitudinal shower development near the beginning of showers where photons and  $\pi^0$ s differ statistically. The third layer spans the region of maximum EM shower energy deposits and the fourth completes the EM coverage of approximately 20 radiation lengths. The fine-hadronic modules are typically segmented into three or four layers. Typical transverse sizes of towers in both EM and hadronic modules are  $\Delta\eta = 0.1$  and  $\Delta\phi = 2\pi/64 \approx 0.1$ . The third section of EM modules is twice as finely segmented in both  $\eta$  and  $\phi$  to allow more precise determination of EM shower centroids.

The CC has a length of 2.6 m covering the pseudorapidity region  $|\eta| < 1.2$  and consists of three concentric cylindrical rings. There are 32 EM modules in the inner ring, 16 FH modules in the surrounding ring, and 16 CH modules in the outer ring. The EM, FH and CH module boundaries are rotated so that no projective ray encounters more than one intermodule gap.

The two mirror-image end calorimeters (ECN and ECS) contain four module types. To avoid the dead spaces in a multi-module design, there is just one EM module and one inner hadronic (IH) module. Outside the EM and IH, there are concentric rings of 16 middle and outer (MH and OH) modules. The azimuthal boundaries of the MH and OH modules are offset to prevent cracks through which particles could penetrate the calorimeter. This makes the DØ detector almost completely hermetic and allows for a very accurate measurement of missing transverse energy. Due to increase in the background and loss of the tracking efficiency at  $|\eta| > 2.5$ , the electron and photon candidates are restricted to  $1.5 < |\eta| < 2.5$  in the EC.

In the transition region between the CC and EC ( $0.8 \leq |\eta| \leq 1.4$ ), there is a large amount of uninstrumented material in the form of cryostat walls, stiffening rings, and module endplates. To correct for energy deposited in the uninstrumented material there are two scintillation counter arrays, of segmentation  $0.1 \times 0.1$ , called intercryostat detectors (ICD). In addition, separate single-cell structures called massless gaps (MG) are mounted on the end plates of the CCFH modules and on the front plates of ECMH and ECOH modules.

The Main Ring beam pipe passes through the outer layers of the CC, ECN and ECS. Beam losses from the Main Ring cause energy deposition in the calorimeter that bias the energy measurement. The data acquisition system stops recording data during periods of Main Ring activity near the DØ detector or flags the events.

### C. Muon Detectors

The DØ muon detector, located outside the calorimeter, is divided in two subsystems: the Wide Angle Muon Spectrometer and the Small Angle Muon Spectrometer. The purpose of this system is the identification of muons produced in  $p\bar{p}$  collisions and the determination of their trajectories and momenta. Since the calorimeter is thick enough to absorb the debris

from electromagnetic and hadronic showers, muons can be identified with high purity. The muon system is not used in this analysis and is not discussed further here.

### III. MULTILEVEL TRIGGER AND DATA ACQUISITION SYSTEM

The trigger system for the D $\emptyset$  detector is a multilayer hierarchical system with increasingly complex tests applied to the data at each successive stage to reduce the sample of events.

The first stage, called level 0 (L0), consists of two scintillator arrays mounted on the front surfaces of the EC cryostats perpendicular to the beam direction. Each array partially covers a region in pseudorapidity of  $1.9 < |\eta| < 4.3$ , with nearly complete coverage over the range  $2.2 < |\eta| < 3.9$ . The L0 system is used to detect the occurrence of an inelastic  $p\bar{p}$  collision and serves as the luminosity monitor for the experiment. In addition, it provides fast information on the  $z$ -coordinate of the primary collision vertex, by measuring the difference in arrival time between particles hitting the north and south L0 arrays, for use in early trigger decisions. A slower, more accurate measurement of the position of the interaction and indication of the occurrence of multiple interactions are available for subsequent trigger decisions. The L0 trigger is  $\approx 99\%$  efficient for non-diffractive inelastic collisions. The output rate from L0 is on the order of 150 kHz at a typical luminosity of  $1.6 \times 10^{31} \text{ cm}^{-2} \text{ s}^{-1}$ .

The next stage is called the level 1 trigger (L1). It is responsible for combining the results from individual L1 components into a set of global decisions that commands the readout of the digitization crates, and interacts with the next stage, the level 2 trigger (L2). Most of these components, such as the L1 calorimeter triggers and the muon triggers, operate within the  $3.5 \mu\text{s}$  interval between beam crossings so that no events go unexamined. However, some other components, such as the TRD trigger and some components of the calorimeter and muon triggers, called the level 1.5 trigger (L1.5), may require more time. The goal of the L1 trigger is to reduce the event rate from the beam crossing rate to 100–200 Hz. The primary input for the L1 trigger consists of 256 trigger terms, each of which is a single bit indicating that some specific requirement is met. These 256 terms are reduced to a set of 32 L1 trigger bits by a two-dimensional AND-OR network. An event is said to pass L1 if at least one of these 32 bits is set. The L1 trigger also uses information about Main Ring activity. To prevent the saturation of the trigger system due to the large cross sections of some process such as QCD multijet events, the L1 trigger can be prescaled.

The L1 calorimeter trigger covers up to  $|\eta| < 4.0$  in trigger towers of  $0.2 \times 0.2$  in  $\eta - \phi$  space. These towers are subdivided longitudinally into electromagnetic and hadronic trigger towers. The output of the calorimeter L1 trigger is the transverse energy deposited in these towers.

For the 1993–1995 collider run, a L1.5 trigger for the calorimeter was implemented using the L1 calorimeter trigger tower data and applying filters based on neighbor sums and ratios of the EM and EM plus hadronic transverse energies.

When an event satisfies the L1 trigger, the event data are passed on the D $\emptyset$  data acquisition pathways to a farm of 48 parallel microprocessors, which serve as event builders as

well as the L2 trigger system. The L2 system collects the digitized data from all relevant detector elements and trigger blocks for events that successfully pass the Level 1 triggers. It applies sophisticated algorithms to the data to reduce the event rate to about 2 Hz before passing events on to the host computer for event monitoring and recording. All the data for a specific event are sent over parallel paths to memory modules in a specific, selected node. The event data are collected and formatted in final form in the node, and the L2 filter algorithms are executed.

The L2 filtering process in each node is built around a series of filter tools. Each tool has a specific function related to the identification of a type of particle or event characteristic. There are tools to recognize jets, muons, calorimeter EM clusters, tracks associated with calorimeter clusters,  $\sum E_T$ , and  $\cancel{E}_T$ . Other tools recognize specific noise or background conditions. There are 128 L2 filters available. If all of the L2 requirements (for at least one of these 128 filters) are satisfied, the event is said to pass L2 and it is temporarily stored on disk before being transferred to an 8 mm magnetic tape.

Once an event is passed by an L2 node, it is transmitted to the host cluster, where it is received by the data logger, a program running on one of the host computers. This program and others associated with it are responsible for receiving raw data from the L2 system and copying it to magnetic tape, while performing all necessary bookkeeping tasks (e.g. time stamps, run number, and output event number, etc.). Some data are also sent to an event pool for online monitoring.

### A. Electron Trigger

To trigger on electrons, L1 requires the transverse energy in the EM section of a trigger tower to be above a programmable threshold. The L2 electron algorithm uses the full segmentation of the EM calorimeter to identify electron showers. Using the trigger towers that were above threshold at L1 as seeds, the algorithm forms clusters which include all cells in the four EM layers and the first FH layer in a region of  $\Delta\eta \times \Delta\phi = 0.3 \times 0.3$ , centered around the tower with the highest  $E_T$ . The longitudinal and transverse energy profile of the cluster must satisfy the following requirements: (i) the fraction of the cluster energy in the EM section (the EM fraction) must be above a threshold dependent on energy and detector position; and (ii) the difference between the energy depositions in two regions in the third layer, covering  $\Delta\eta \times \Delta\phi = 0.25 \times 0.25$  and  $0.15 \times 0.15$  and centered on the cell with the highest  $E_T$ , must be within a window which depends on the total cluster energy.

### B. Jet Trigger

The L1 jet triggers require the sum of the transverse energy in the EM and FH sections of a trigger tower to be above a programmable threshold. The L2 jet algorithm begins with an  $E_T$ -ordered list of towers that are above threshold at L1. At L2, a jet is formed by placing a cone of given radius  $\mathcal{R}$ , where  $\mathcal{R} = \sqrt{\Delta\eta^2 + \Delta\phi^2}$ , around the seed tower from L1.

If another seed tower lies within the jet cone, it is passed over and not allowed to seed a new jet. The summed  $E_T$  in all of the towers included in the jet cone defines the jet  $E_T$ . If any two jets overlap, then the towers in the overlap region are added into the jet candidate which was formed first. To filter events, requirements on several quantities can be imposed. These are the minimum transverse energy of a jet, the minimum transverse size of a jet, the minimum number of jets, and fiducial requirements on the pseudorapidity of the jets.

### C. Missing Transverse Energy Trigger

Many rare and interesting physics processes involve production of weakly interacting particles such as neutrinos. These particles can not be directly detected with a conventional collider detector. However, conservation of momentum from the initial to final state implies that the momenta of such particles can be inferred from the vector sum of the momenta of the particles which are detected. Since the energy flow near the beamline is largely undetected, this method can only be used in the plane transverse to the beam. The negative vector sum of the momenta of the detected particles is referred as missing  $E_T$  and denoted by  $\cancel{E}_T$ ; it is used as an indicator of the presence of weakly interacting particles. At L2,  $\cancel{E}_T$  is computed using the vector sum of all calorimeter and ICD cell energies with respect to the  $z$  position of the interaction vertex, which is determined from the timing of the hits in the L0 counters.

## IV. PARTICLE IDENTIFICATION

### A. Electron

Electrons are identified by the properties of the shower in the calorimeter. The algorithm loops over all EM towers with  $E > 50$  MeV, and connects the neighboring tower with the highest energy. The cluseter energy is then calculated as the sum of the energies in the towers and the energies in the corresponding FH1 layers. The ratio of the energy in the EM cluster and the energy in the EM cluster plus the energy summed over corresponding hadronic layers (the EM fraction) is used to discriminate electrons and photons from hadronic showers. A cluster must pass the following criteria to be an electron/photon candidate: (i) the EM fraction must be greater than 90% and (ii) at least 40% of the energy must be contained in a single tower. To distinguish electrons from photons, we search for a track in the central detector that points to the EM cluster from the primary interaction vertex within a window of  $|\Delta\eta| \leq 0.1$ , and  $|\Delta\phi| \leq 0.1$ . If one or more tracks are found, the object is classified as an electron candidate. Otherwise, it is classified as a photon candidate.

#### 1. Selection Requirements

The spatial development of EM showers is quite different from that of hadronic showers and the shower shape information can be used to differentiate electrons and photons from

hadrons. The following variables are used to select the electrons:

- (i) Electromagnetic energy fraction. This quantity is based on the observation that electrons deposit almost all of their energy in the EM section of the calorimeter, while hadrons are typically much more penetrating (only 10% of their energy is deposited in the EM section of the calorimeter), and is defined as the ratio of EM energy to the total shower energy. All the electrons in this analysis are required to have at least 95% of their total energy in the EM calorimeter. This requirement is about 99% efficient.
- (ii) Covariance matrix ( $H$ -matrix)  $\chi^2$ . The shower shape may be characterized by the fraction of the cluster energy deposited in each tower in each layer of the calorimeter. These fractions are correlated, i.e., an electron shower deposits energies following the well-known transverse and longitudinal shapes of the EM shower and a hadron shower following the shapes of the hadronic shower. To obtain a good discrimination against hadrons, we use a covariance matrix technique. The observables in this technique are the fractional energies in layers 1, 2, and 4 of the EM calorimeter and the fractional energy in each cell of a  $6 \times 6$  array of cells in layer 3 centered on the most energetic tower in the EM cluster. To take into account the dependence on the energy and the position of the primary interaction vertex, we use the logarithm of the shower energy and the position of the event vertex along the beam axis as observables. In this analysis, the event vertex is determined by extrapolating CDC tracks to the  $z$  axis. The vertex associated with the highest number of tracks is used for a multiple-vertex event. The covariance matrices with these 41 variables are built for each of the 37 detector towers (located at different values of  $\eta$ ) using Monte Carlo electrons. The Monte Carlo was tuned to agree with our test beam measurements of the shower shapes. Comparison is done by calculating a  $\chi^2$  for the 41 observables of the shower in question using the covariance matrices. In this analysis we require that the  $\chi^2$  be less than 100 for CC electron candidates and less than 200 for EC electrons. This requirement is about 95% efficient.
- (iii) Isolation. The decay electron from a  $W$  boson should not be close to any other object in the event. This is quantified by the isolation fraction. Let  $E(0.4)$  be the energy deposited in all calorimeter cells in the cone  $\mathcal{R} < 0.4$  around the electron direction and  $EM(0.2)$  the energy deposited in the EM calorimeter in the cone  $\mathcal{R} < 0.2$ . The isolation variable is then defined as the ratio  $\mathcal{I} = [E(0.4) - EM(0.2)]/EM(0.2)$ . The requirement  $\mathcal{I} < 0.1$  is approximately 97% efficient.
- (iv) Track match significance. An important source of background for electrons is photons from the decay of  $\pi^0$  or  $\eta$  mesons. Such photons do not leave tracks in the central detector, but might appear to do so if a charged particle is nearby. This background can be reduced by demanding a good spatial match between calorimeter energy cluster and nearby tracks. The significance  $S$  of the mismatch between these quantities is given by  $S = [(\Delta\phi/\delta_{\Delta\phi})^2 + (\Delta z/\delta_{\Delta z})^2]^{1/2}$ , where  $\Delta\phi$  is the azimuthal mismatch,  $\Delta z$  the mismatch along the beam axis, and  $\delta_x$  is the resolution of the observable  $x$ . This form is appropriate for the central calorimeter. For the end calorimeter,  $r$  replaces  $z$ . Requiring  $S < 5$  is 95(78)% efficient for CC(EC) electrons.
- (v) Track-in-road. All the electrons are required to have a reconstructed track somewhere in the tracking road between the calorimeter energy cluster and the vertex to enter the

$W \rightarrow e\nu$  sample. For this analysis, this requirement is found to be 84(86)% efficient for CC(EC) electrons.

For this analysis we combine these quantities to form the electron identification criteria. A summary of the selection requirements used and their efficiencies are listed in Table I.

TABLE I. Electron selection requirements and their efficiencies.

Selection requirement	CC		EC	
		$\varepsilon$		$\varepsilon$
$H$ -matrix $\chi^2$	< 100	$0.946 \pm 0.005$	< 200	$0.950 \pm 0.008$
EM fraction	> 0.95	$0.991 \pm 0.003$	> 0.95	$0.987 \pm 0.006$
Isolation	< 0.10	$0.970 \pm 0.004$	< 0.10	$0.976 \pm 0.007$
Track match	< 5	$0.948 \pm 0.005$	< 5	$0.776 \pm 0.012$
Track-in-road		$0.835 \pm 0.009$		$0.858 \pm 0.006$

## 2. Electromagnetic Energy Corrections

The energy scales of the calorimeters were originally set using test-beam calibration data. However, due to differences in conditions between the test-beam setup and the DØ installation, additional corrections are needed.

The EM energy scales for the calorimeters have been determined by comparing the measured masses of  $\pi^0 \rightarrow \gamma\gamma$ ,  $J/\psi \rightarrow ee$ , and  $Z \rightarrow ee$  to their known values. If the electron energy measured in the calorimeter and the true energy are related by  $E_{\text{meas}} = \alpha E_{\text{true}} + \delta$ , the measured and true mass values are, to first order, related by  $m_{\text{meas}} = \alpha m_{\text{true}} + \delta f$ . The variable  $f$  depends on the decay topology. To determine  $\alpha$  and  $\delta$  we fit the Monte Carlo prediction to the observed resonances with  $\alpha$  and  $\delta$  as free parameters [21]. The values of  $\alpha$  and  $\delta$  are found to be  $\alpha = 0.9533 \pm 0.0008$  and  $\delta = -0.16^{+0.03}_{-0.21}$  GeV for the CC and  $\alpha = 0.952 \pm 0.002$  and  $\delta = -0.1 \pm 0.7$  GeV for the EC.

## 3. Energy Resolution

The energy resolution of electrons and photons for the CC is expressed by the empirical relation  $\left(\frac{\sigma}{E}\right)^2 = C^2 + \frac{S^2}{E_T} + \frac{N^2}{E^2}$ , where  $E$  is the energy of the incident electron,  $C$  is a constant term due to calibration errors,  $S$  is the sampling fluctuation of the liquid argon calorimeter, and  $N$  corresponds to the noise term. The  $E_T$  in the relation is replaced by  $E$  for the EC. The sampling term and noise term are obtained from test beam results. The noise term from test beam is found to agree with the one obtained in the collider environment based on the width of the pedestal distributions. The constant term is tuned to match the mass resolution of observed and simulated  $Z \rightarrow ee$  events. Table II lists these parameters.

TABLE II. Energy resolution parameters for electrons and photons.

Quantity	CC	EC
$C$	0.017	0.009
$S$ ( $\sqrt{\text{GeV}}$ )	0.14	0.157
$N$ (GeV)	0.49	1.140

## B. Jets

In this analysis, jets are reconstructed using a fixed-cone algorithm. This algorithm uses a fixed-cone radius  $\mathcal{R} = \sqrt{\Delta\eta^2 + \Delta\phi^2}$ . The algorithm forms preclusters of contiguous cells out to a radius of  $\mathcal{R}_{\text{precluster}} = 0.3$  around the highest  $E_T$  tower. Only towers with  $E_T > 1$  GeV are included in preclusters. These preclusters become the starting point for jet reconstruction. An  $E_T$ -weighted center of gravity is then formed using the  $E_T$  of all towers within a radius  $\mathcal{R}$  of the center of the cluster, and the process is repeated until the jet becomes stable. A jet must have  $E_T > 8$  GeV. If two jets share energy, they are combined or split, based on the fraction of energy shared relative to the  $E_T$  of the lower  $E_T$  jet. If the shared fraction exceeds 50%, the jets are combined.

A cone radius of  $\mathcal{R} = 0.5$  is used in this analysis. The  $\mathcal{R} = 0.3$  cone algorithm is more efficient compared to wider cone sizes which cause undesired jet merging for high- $p_T$   $W$  or  $Z$  bosons. However, due to the relatively large uncertainties in the jet-energy measurement of the  $\mathcal{R} = 0.3$  cone algorithm with energy flowing out of the cone or unnecessary splitting of jets, we choose to use the  $\mathcal{R} = 0.5$  cone algorithm for our studies.

### 1. Selection Requirements

To remove fake jets produced by cosmic rays, calorimeter noise, and backgrounds from the Main Ring, we have developed a set of requirements based on a detailed study of Monte Carlo events, noise data taken with no colliding beam, and colliding beam data sets. The variables used are:

(i) Electromagnetic energy fraction ( $emf$ ). As for electrons, this quantity is defined as the fraction of energy deposited in the electromagnetic section of the calorimeter. A requirement on this quantity is imposed to remove electrons, photons and fake jets from the jet sample. Electrons and photons typically have a high EM fraction. Fake jets are caused by the background from the Main Ring beam or by hot cells, and therefore do not have energy depositions in the EM section, resulting in a low EM fraction. Jets in general leave energy in both the electromagnetic and hadronic sections of the calorimeter. Jets with  $0.05 < emf < 0.95$  are defined as good jets.

(ii) Hot cell energy fraction ( $hcf$ ). The  $hcf$  is defined as the ratio of the energy of the second highest  $E_T$  cell to the energy of the highest  $E_T$  cell within a jet. A requirement on

this quantity is imposed to remove calorimeter noise. Hot cells appear when a discharge occurs between cell electrodes; neighboring cells are unaffected. In this case,  $hcf$  is small. The  $hcf$  for a jet should not be small since the energy in a jet is expected to be spread over a number of cells. If most of the energy is concentrated in only one cell, it is very likely to be a false jet reconstructed from discharge noise. For good jets,  $hcf$  is found to be greater than 0.1.

(iii) Coarse hadronic energy fraction ( $chf$ ). This quantity is defined as the fraction of jet energy deposited in the coarse hadronic section of the calorimeter. A requirement on this quantity is imposed to remove activity caused by the Main Ring. The Main Ring at DØ passes through the CH modules and any energy deposition related to it will be concentrated in this section of the calorimeter. Fake jets due to Main Ring activity tend to have more than 40% of their energy in the CH region, while real jets have less than 10% of their energy in this section of the calorimeter. Therefore good jets are required to have  $chf < 0.4$ .

## 2. Hadronic Energy Corrections

Since the measured jet energy usually is not equal to the energy of the original parton which formed the jet, corrections are needed to avoid systematic biases. There are several effects which contribute to the jet energy response; they are non-uniformities in the calorimeter, non-linearities in the calorimeter response to hadrons, out-of-cone showering, noise due to the radioactivity of uranium, and energy from the products of soft interactions of spectator partons within the proton and the antiproton (underlying event). The first two effects are estimated using a method called Missing  $E_T$  Projection Fraction (MPF) [22].

The MPF method starts by looking for events with an isolated EM cluster due to a photon or a jet which fragmented mostly into neutral mesons, a hadronic jet lying opposite in  $\phi$ , and no other object in the event. The EM cluster energy is corrected using the electromagnetic energy corrections described above. There should be no energetic neutrinos in these events so that any missing transverse energy remaining in the event can be attributed to a mismeasurement of the hadronic jet. Projecting the  $E_T$  along the jet axis, corrections for the jet can be determined. This is averaged over similar jets in the sample to obtain a correction which is a function of jet  $E_T$ ,  $\eta$ , and electromagnetic content.

The effect due to out-of-cone showering is estimated using Monte Carlo event samples. The effects due to underlying events and the uranium noise are determined in separate studies using minimum bias event data. The minimum bias data is the inclusive inelastic collision event sample triggered by L0 only.

## 3. Energy Resolution

The jet energy resolution has been studied using dijet momentum balance. The empirical formula for the jet energy resolution is  $\left(\frac{\sigma}{E}\right)^2 = C^2 + \frac{S^2}{E^2} + \frac{N^2}{E^2}$ , where  $C$  is the error term from the calibration,  $S$  represents the shower fluctuations in the sampling gaps, and  $N$  denotes

the contribution due to noise and the underlying event. Table III shows the resolution parameters for each of the calorimeter  $\eta$  regions.

TABLE III. Jet energy resolution parameters for each of the calorimeter regions.

$\eta$ Region	Noise Term $N$	Sampling Term $S$ ( $\sqrt{\text{GeV}}$ )	Constant Term $C$ (GeV)
$ \eta  < 0.5$	$7.07 \pm 0.09$	$0.81 \pm 0.02$	$0.00 \pm 0.01$
$0.5 <  \eta  < 1.0$	$6.92 \pm 0.09$	$0.91 \pm 0.02$	$0.00 \pm 0.01$
$1.0 <  \eta  < 1.5$	$0.00 \pm 1.40$	$1.45 \pm 0.02$	$0.05 \pm 0.01$
$1.5 <  \eta  < 2.0$	$8.15 \pm 0.21$	$0.48 \pm 0.07$	$0.00 \pm 0.01$
$2.0 <  \eta  < 3.0$	$3.15 \pm 2.50$	$1.64 \pm 0.13$	$0.01 \pm 0.58$

### C. Neutrinos: Missing Transverse Energy

The presence of neutrinos in an event is inferred from the  $\cancel{E}_T$ . In this analysis we have assumed that the  $\cancel{E}_T$  in each event corresponds to the neutrino in the  $W \rightarrow e\nu$  decay.

#### 1. Missing $E_T$

The missing transverse energy in the calorimeter is defined as  $\cancel{E}_T = (\cancel{E}_{T_x}^2 + \cancel{E}_{T_y}^2)^{1/2}$ , where  $\cancel{E}_{T_x} = -\sum_i E_i \sin(\theta_i) \cos(\phi_i) - \sum_j \Delta E_x^j$  and  $\cancel{E}_{T_y} = -\sum_i E_i \sin(\theta_i) \sin(\phi_i) - \sum_j \Delta E_y^j$ . The first sum (over  $i$ ) is over all cells in the calorimeter, ICD and MG. The second sum (over  $j$ ) is over the  $E_T$  corrections applied to all electrons and jets in the event. This quantity can be used to estimate the transverse energy of the neutrinos in events without muons which only deposit a small portion of their energy in the calorimeter. Therefore the total missing  $E_T$  is actually the calorimeter missing  $E_T$  with the transverse momenta of muon tracks subtracted. Since in this analysis we do not use muons, we will refer to the calorimeter  $\cancel{E}_T$  as the  $\cancel{E}_T$ .

#### 2. $\cancel{E}_T$ Resolution

An ideal hermetic detector would measure the magnitude of the  $\cancel{E}_T$  vector as zero for events with no real source of  $\cancel{E}_T$ . However, detector noise and energy resolution in the measurement of jets, photons, electrons and muons contribute to some amount of  $\cancel{E}_T$ . In addition, dead regions or non-uniformity of response in the detector also result in  $\cancel{E}_T$ . Therefore it is important to measure this contribution of  $\cancel{E}_T$  to gauge the sensitivity of the detector to real  $\cancel{E}_T$ . The  $\cancel{E}_T$  resolution is parameterized as  $\sigma = 1.08\text{GeV} + 0.019(\sum E_T)$ , which is obtained using minimum bias data. The  $\sum E_T$  is used for this parameterization since one

would expect that the greater the total amount of transverse energy in the event, the larger the possible mismeasurement of the balance.

## V. DATA SAMPLE

The analysis of the  $WW/WZ \rightarrow e\nu jj$  process is based on the data sample taken during the 1993–1995 Tevatron Collider run (called Run 1b). The L0 trigger examines the presence of an inelastic collision and is not included in the trigger conditions for the  $W$  boson data sample, in order to allow studies of diffractive  $W$  boson production. This analysis uses a subset of the  $W \rightarrow e\nu$  data sample and the requirement that the L0 trigger is satisfied is imposed offline. The L1 trigger for the data sample used in this analysis (called the `EM1_1_HIGH` trigger) requires the presence of an electromagnetic trigger tower with  $E_T > 10$  GeV. The L1.5 trigger then requires the L1 trigger tower to have  $E_T > 15$  GeV. This trigger also examines whether the electromagnetic fraction is greater than 85%. The L2 trigger for the data sample used in this analysis (called the `EM1_EISTRKCC_MS` trigger) requires an electron candidate with  $E_T > 20$  GeV that has a shower shape consistent with that of an electron and is isolated from other objects in the calorimeter and  $\cancel{E}_T > 15$  GeV.

Additional conditions are imposed on the data sample to further reduce unwanted events. Triggers which occur at the times when a Main Ring proton bunch passes through the detector are not used in this analysis. Similarly, triggers which occur during the first 0.4 seconds of the 2.4-second antiproton production cycle are vetoed. Data taken during periods when the data acquisition system or the detector sub-systems had problems (called bad runs) are also discarded. The integrated luminosity of the data sample with these trigger requirements is estimated to be  $82.3 \pm 4.4 \text{ pb}^{-1}$  [23]. The efficiency and turn-on curves of the L2 trigger for the data sample are described in Ref. [24]. The trigger efficiency is  $(98.1 \pm 1.9)\%$ .

Data samples that satisfy other L2 triggers (the `EM1_ELE_MON` and `ELE_1_MON` triggers) are used for background studies. These triggers select events that have an electron candidate with  $E_T > 20$  GeV and  $E_T > 16$  GeV, respectively. The electron candidates must pass the shower shape requirements, but not the isolation requirement. These triggers use the same L1 and L1.5 conditions as the signal trigger.

## VI. EVENT SELECTION

The  $WW/WZ \rightarrow e\nu jj$  candidates are selected by searching for events with an isolated high- $E_T$  electron, large  $\cancel{E}_T$ , and at least two high- $E_T$  jets. Electrons in the candidate sample must be in the fiducial region  $|\eta| < 1.1$  and away from the calorimeter module boundaries in  $\phi$  ( $\Delta\phi > 0.01$ ), or within the fiducial region  $1.5 < |\eta| < 2.5$ . Jets in the candidate sample must be in the fiducial region  $|\eta| < 2.5$ .

The  $W \rightarrow e\nu$  decay is identified by one and only one isolated electron with  $E_T > 25$  GeV and  $\cancel{E}_T > 25$  GeV in the event. The transverse mass of the electron and neutrino

system is required to be  $M_T > 40 \text{ GeV}/c^2$ , where  $M_T = \{2E_T^e \cancel{E}_T [1 - \cos(\phi_e - \phi_\nu)]\}^{1/2}$ . The requirement on the electron  $E_T$  ( $E_T^e > 25 \text{ GeV}$ ) is high enough to avoid the leading edge of the trigger turn-on curve which has a hardware threshold of  $20 \text{ GeV}$ . The requirement of only one electron reduces background from  $Z$  boson production. The requirements on  $\cancel{E}_T$  and  $M_T$  reduce the background contribution from misidentified electrons.

The  $W/Z \rightarrow jj$  decay is identified by requiring at least two jets with  $E_T^j > 20 \text{ GeV}$  in the event and that the invariant mass of the two-jet system be consistent with that of the  $W$  or  $Z$  boson ( $50 < M_{jj} < 110 \text{ GeV}/c^2$ ). The dijet invariant mass ( $M_{jj}$ ) is calculated by  $M_{jj} = \{2E_T^{j1} E_T^{j2} [\cosh(\eta_{j1} - \eta_{j2}) - \cos(\phi_{j1} - \phi_{j2})]\}^{1/2}$ . If there are more than two jets in the event, the two jets with the highest dijet invariant mass formed from the three leading jets are used.

The difference between the  $p_T$  values of the  $e\nu$  and the two-jet systems is used to reduce backgrounds. For  $W$  boson pair production events, the  $p_T(e\nu) - p_T(jj)$  distribution should be peaked at zero and have a symmetric Gaussian shape. The width of the Gaussian distribution is determined primarily by the jet energy resolution. On the other hand, for the background events from the  $t\bar{t}$  production, the distribution should have a positive average value and a broader and asymmetric shape due to additional  $b$ -quark jets in the events. We require  $|p_T(e\nu) - p_T(jj)| < 40 \text{ GeV}/c$ .

The data satisfying the above selection criteria yield 399 events. Figure 4 (upper plot) shows the scatter plot of  $p_T(e\nu)$  vs  $p_T(jj)$  for candidate events that satisfy the two-jet mass requirement. The width of the band reflects both the resolution and  $p_T$  of the  $e\nu jj$  system. The lower plot shows the scatter plot of  $p_T(e\nu)$  vs  $M_{jj}$  without the mass requirement.

## VII. DETECTION EFFICIENCY

### A. Electron Selection Efficiency

The efficiencies of the electron selection requirements have been studied using the  $Z \rightarrow ee$  event sample from the 1993–1995 Tevatron collider run taken with the `EM2_EIS_HI` trigger. These events were selected using L1 and L1.5 triggers that required two EM towers with  $E_T > 7 \text{ GeV}$  at L1, and at least one tower with  $E_T > 12 \text{ GeV}$  and 85% of its energy in the EM section of the calorimeter. At L2 the trigger required two electron candidates with  $E_T > 20 \text{ GeV}$  that satisfied electron shower shape and isolation requirements. To select an unbiased sample of electrons, we use events in which one of the electrons passes the tag quality requirements: EM fraction  $> 0.90$ , Isolation  $< 0.15$ ,  $H$ -matrix  $\chi^2 < 100(200)$  for CC(EC), and track match significance  $< 10$ . The second electron in the event is then assumed to be unbiased. A given event may contribute twice to the sample, if both electrons pass the tag requirements. The efficiency of a selection requirement for electrons is given by  $\varepsilon = (\varepsilon_s - \varepsilon_b f_b) / (1 - f_b)$ , where  $\varepsilon_s$  is the efficiency measured in the signal region,  $\varepsilon_b$  is the efficiency measured in the background region, and  $f_b$  is the ratio of the number of background events in the signal region to the total number of events in the signal region. The signal region is defined as the region of the  $Z$  boson mass peak ( $86 < m_{ee} < 96 \text{ GeV}/c^2$ ).

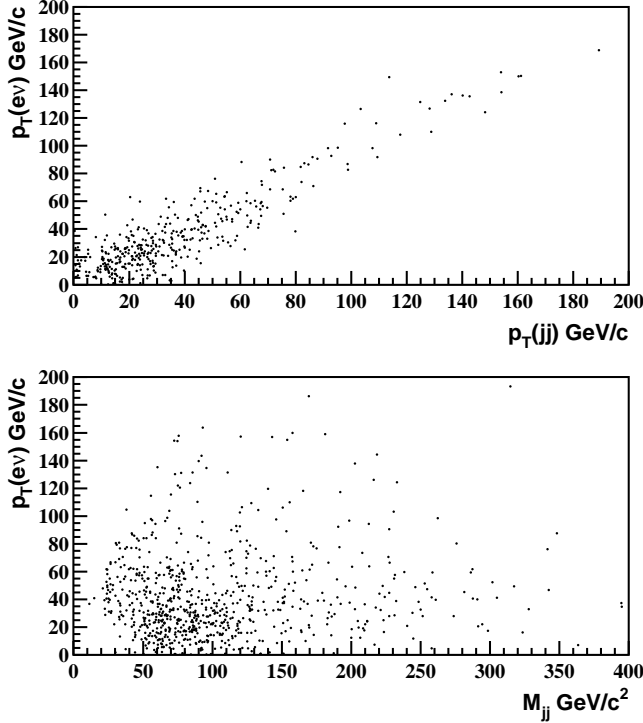


FIG. 4. Scatter plots of  $p_T(e\nu)$  vs  $p_T(jj)$  (top plot) and  $p_T(e\nu)$  vs  $M_{jj}$  (bottom plot).

The background regions are defined as  $(61 < m_{ee} < 71 \text{ GeV}/c^2)$  and  $(111 < m_{ee} < 121 \text{ GeV}/c^2)$ . We determine  $f_b$  in the signal region using an average of the number of events in the background regions. The systematic uncertainties on the efficiencies are estimated from a comparison with the efficiencies obtained using an alternative method which fits the invariant mass spectrum of two electrons to a Breit-Wigner curve convoluted with a Gaussian plus a linear background. The efficiencies from the two methods agree well. The track-in-road efficiency is estimated in a similar manner, except that EM clusters with no matching track are also included as the unbiased electrons in the sample. Table I summarizes the electron efficiencies.

### B. $W/Z \rightarrow jj$ Selection Efficiency

The  $W/Z \rightarrow jj$  selection efficiency is estimated using Monte Carlo  $WW/WZ \rightarrow e\nu jj$  events generated with the ISAJET [25] and PYTHIA [26] programs, followed by a detailed simulation of the DØ detector, and is parametrized as a function of  $p_T^W$ . We use several samples generated with different  $W/Z$  boson  $p_T$  thresholds to improve the statistics of the high- $p_T$   $W/Z$  boson samples. Figure 5 shows the  $W/Z \rightarrow jj$  detection efficiency  $\epsilon(W \rightarrow jj)$  calculated as the ratio of the events after the two-jet selection requirement to the initial number of events. At low  $p_T$ , the detection efficiency is superficially elevated due to jets from the initial- and final-state radiation (ISR/FSR) identified as jets from a  $W$  or a  $Z$  boson. On the other hand, the decrease in the efficiency at high  $p_T$  is due to two jets from

a  $W$  or a  $Z$  boson merging to one. The efficiencies obtained from **ISAJET** are tabulated and used to estimate the efficiencies for identifying the  $WW/WZ$  process.

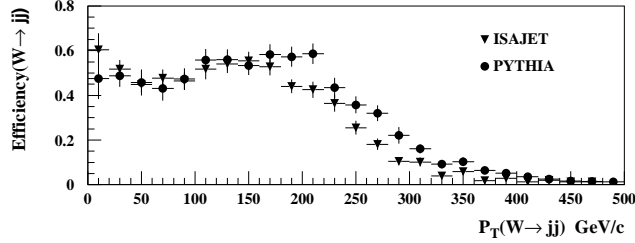


FIG. 5. Efficiency for  $W \rightarrow jj$  selection as a function of  $p_T^W$ . The decrease in the efficiency at high  $p_T$  is due to two jets from  $W$  boson merging to one.

The  $W/Z \rightarrow jj$  efficiency estimation is affected by the jet energy scale, the accuracy of the ISR/FSR simulation, the accuracy of the parton fragmentation mechanism, and the statistics of the Monte Carlo event samples.

The calorimeter energy scale correction has an uncertainty that decreases from 5% at jet  $E_T = 20$  GeV to 2% at 80 GeV and then increases to 5% at 350 GeV. The effect of this uncertainty has been studied by recalculating the efficiency with the jet energy scale changed by one standard deviation. The largest relative change in the accepted number of events is found to be 3%.

To estimate the uncertainty due to the accuracy of the ISR/FSR simulation or parton fragmentation mechanism, we also calculate the  $W/Z \rightarrow jj$  efficiency using Monte Carlo event samples generated with the **PYTHIA** event generator. We find that the efficiency obtained using **ISAJET** is lower than that obtained with **PYTHIA**. The relative change in the numbers of accepted events is less than 10%. We have chosen to use the efficiencies obtained from **ISAJET** because they lead to smaller estimates of the  $WW/WZ$  cross section and therefore conservative limits on the anomalous couplings. We use one-half of the largest difference in these two efficiency estimations as the systematic uncertainty due to the event generator (5%).

### C. Overall Selection Efficiency

The overall detection efficiency of the  $WW/WZ \rightarrow e\nu jj$  events with the SM couplings is calculated using two MC methods and the electron selection and trigger efficiencies measured from data. The first MC method uses the **ISAJET** event generator followed by the detailed detector simulation of D $\emptyset$  detector. The second MC method uses the event generator of Ref. [2] and a fast detector simulation program.

Using **ISAJET** and the CTEQ2L [27] parton distribution function, followed by a full simulation of the detector, we generated 2500  $WW \rightarrow e\nu jj$  events and 1000  $WZ \rightarrow e\nu jj$  events with SM couplings. The event selection efficiency is estimated to be  $\epsilon_{WW} = (13.4 \pm 0.8)\%$  for the  $WW \rightarrow e\nu jj$  signal, and  $\epsilon_{WZ} = (15.7 \pm 1.4)\%$  for the  $WZ \rightarrow e\nu jj$  signal. The errors are statistical only. The combined efficiency for  $WW/WZ \rightarrow e\nu jj$  is given by  $[\epsilon_{WW} \cdot \sigma \cdot B(WW \rightarrow$

$e\nu jj) + \epsilon_{WZ} \cdot \sigma \cdot B(WZ \rightarrow e\nu jj)] / [\sigma \cdot B(WW \rightarrow e\nu jj) + \sigma \cdot B(WZ \rightarrow e\nu jj)] = (13.7 \pm 0.7)\%$ . The theoretical cross sections of 9.5 pb for  $WW$  and 2.5 pb for  $WZ$  production [28] and the  $W$  and  $Z$  boson branching fractions by the Particle Data Group [4] are used in this calculation ( $\sigma \cdot B(WW \rightarrow e\nu jj) = 1.38 \pm 0.05$  pb and  $\sigma \cdot B(WZ \rightarrow e\nu jj) = 0.188 \pm 0.006$  pb).

For the fast event simulation, we generated over 30000 events. Approximately four times more events were generated for  $WW$  production than  $WZ$  production, reflecting the theoretical production cross sections of these processes. We calculate the overall detection efficiency for the SM couplings to be  $[14.7 \pm 0.2(\text{stat}) \pm 1.2(\text{syst})]\%$  for  $WW \rightarrow e\nu jj$  and  $[14.6 \pm 0.4(\text{stat}) \pm 1.1(\text{syst})]\%$  for  $WZ \rightarrow e\nu jj$ . The systematic uncertainty (7.8%) includes: statistics of the fast MC (1%), trigger and electron identification efficiency (1%),  $E_T$  smearing and modeling of the  $p_T$  of the  $WW/WZ$  system (5%),  $W \rightarrow jj$  detection efficiencies from the two event generators (5%), and the effect of the jet energy scale (3%). The combined efficiency is  $[14.7 \pm 0.2(\text{stat}) \pm 1.2(\text{syst})]\%$ . Within the errors, the combined efficiency estimated using the fast simulation is consistent with the value obtained using **ISAJET**.

#### D. Expected Number of Signal Events

The expected number of  $WW/WZ \rightarrow e\nu jj$  events with SM couplings is calculated using the above detection efficiencies, the integrated luminosity of the data sample, and the theoretical cross sections.

From the overall detection efficiency obtained with **ISAJET** and the theoretical cross sections, a total of  $17.9 \pm 1.5$  events ( $15.4 \pm 1.4$  events for  $WW$  and  $2.5 \pm 0.2$  events for  $WZ$ ) is expected for  $WW/WZ \rightarrow e\nu jj$  production with SM couplings.

Using the detection efficiency obtained with the event generator of Ref. [2] with a fast detector simulation and  $\sigma \cdot B$  from the event generator ( $\sigma \cdot B(WW \rightarrow e\nu jj) = 1.26 \pm 0.18$  pb, and  $\sigma \cdot B(WZ \rightarrow e\nu jj) = 0.18 \pm 0.03$  pb), we estimate the number of expected SM events to be  $17.5 \pm 3.0$  events ( $15.3 \pm 3.0$   $WW$  events plus  $2.2 \pm 0.5$   $WZ$  events). The uncertainty (17.1%) is the sum in quadrature of the uncertainty in the efficiency above, the uncertainty in the luminosity (5.4%), and that in the NLO calculation (14%).

## VIII. BACKGROUND

There are several sources of background to the  $WW/WZ \rightarrow e\nu jj$  process. They can be divided into two categories based on the nature of the source of the background. One is instrumental background due to misidentified or mismeasured particles, and the other is physics background consisting of physical processes with the same signature as the events of interest.

## A. Instrumental background

The major source of instrumental background is QCD multijet events in which one of the jets showers mainly in the electromagnetic calorimeter and is misidentified as an electron, and the energies of the remaining jets fluctuate enough to cause  $\cancel{E}_T$ . Even though the probability for a jet to be misidentified as an electron is small, the large cross section for QCD multijet events makes this background significant.

The background from QCD multijet events is estimated using samples of *good* and *bad* electrons. A *good* electron event contains an electron with the same quality requirements as described in Sec. IV A 1, while a *bad* electron event contains an EM cluster with EM fraction  $> 0.95$ , Isolation  $\leq 0.15$ , and  $H$ -matrix  $\chi^2 \geq 250$  or track match significance  $\geq 10$ . We assume that the shape of the  $\cancel{E}_T$  spectrum of the events with a bad electron is identical to the  $\cancel{E}_T$  spectrum of the QCD multijet background. Furthermore, with the assumption that the contribution of signal events in the low  $\cancel{E}_T$  region is negligible, the bad electron sample can be normalized to the good electron data in the low  $\cancel{E}_T$  region and the  $\cancel{E}_T$  distribution of the bad electron events can be extrapolated to the signal region of the good electron sample.

To estimate the multijet background, we use triggers without a  $\cancel{E}_T$  requirement. In Run 1b there are several L2 triggers without  $\cancel{E}_T$  requirements. These triggers are `EM1_ELE_MON` and `ELE_1_MON` described in Sec. V. We extract two samples from the data taken with these triggers, based on the electron quality. To avoid biases, we add the requirement that the EM object must pass the same L2 requirements as the signal trigger. The  $\cancel{E}_T$  distribution for the bad electron sample is then normalized to agree with the  $\cancel{E}_T$  distribution for the good electron sample in the low  $\cancel{E}_T$  region ( $\cancel{E}_T < 15$  GeV). Figure 6 shows these two distributions (the good electron sample and the bad electron sample). The normalization factor  $N_F$  is calculated as the ratio of the number of bad electron events to the number of good electron events with  $0 \leq \cancel{E}_T \leq 15$  GeV, after imposing the jet selection requirements on the events, and found to be  $N_F = 1.870 \pm 0.060$  (stat)  $\pm 0.003$  (syst). The systematic uncertainty on the normalization factor is obtained by varying the  $\cancel{E}_T$  range for the normalization from (0,12) GeV to (0,18) GeV.

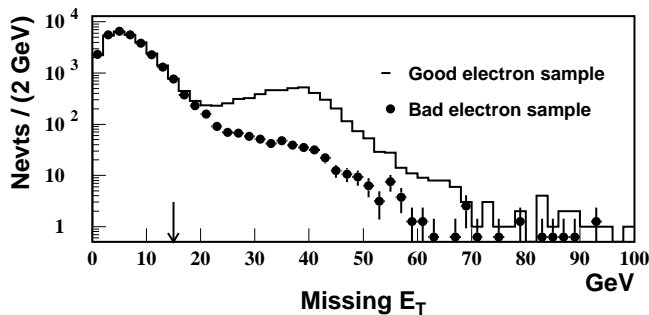


FIG. 6.  $\cancel{E}_T$  distributions for the good electron (histogram) and bad electron (solid circles) samples selected from the data taken with the `EM1_ELE_MON` and `ELE_1_MON` triggers (see text). The bad electron sample is normalized to the good electron sample for  $\cancel{E}_T < 15$  GeV.

In the next step, we select two samples from the data taken with the signal trigger,

one containing background and signal events (*good* electrons that we have obtained in the selection procedure) and the other containing only background events (*bad* electrons). The normalization factor  $N_F$  is then applied to the background only sample. Figure 7 shows the distributions of  $\cancel{E}_T$  for candidates and the estimated QCD multijet background, with the jet requirements imposed.

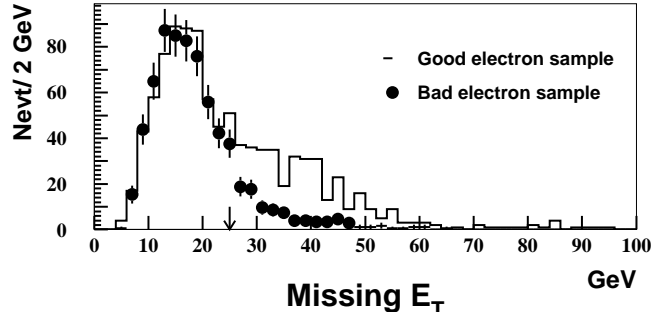


FIG. 7. Distributions of  $\cancel{E}_T$  of the good electron (signal + background) and bad electron (background only) samples selected from the data taken with the signal trigger.

With the procedure described above, we estimate  $104.3 \pm 8.2$  (stat)  $\pm 9.1$  (syst) background events. The systematic uncertainty (8.7%) includes the uncertainty on the normalization factor (1%), the variation when an alternative method is used to estimate this background (5.2%), and the variation for events in  $\cancel{E}_T > 25$  GeV when the  $\cancel{E}_T$  region (15,25) GeV is used for normalization (6.9%). In the alternative method, the probability of a jet being misidentified as an electron is multiplied by the number of multijet events that satisfy the event selection requirements when one of the jets is treated as an electron. When multiple jets in a event satisfy the electron kinematic requirements, the event is treated accordingly. The last contribution estimates the possible contamination of signal in the multijet background sample.

## B. Physics background

The background contribution from physics processes with final state objects identical to those of the signal is estimated using Monte Carlo events.

### 1. $W + \geq 2$ jets

$W + \geq 2$  jets production is the dominant background due to its large cross section. This background is estimated using a Monte Carlo sample generated with the program VECBOS [29] followed by HERWIG [30] for hadronization and then the detailed simulation of the DØ detector. The cross section value from the VECBOS program has a large uncertainty. The  $W + \geq 2$  jets sample generated using VECBOS is therefore normalized to the candidate event sample after subtraction of the QCD multijet background. To avoid the inclusion of real  $WW$  and  $WZ$  events in this procedure, we use only the events whose two-jet invariant

mass lies outside of the  $W$  boson mass peak ( $50 < M_{jj} < 110$   $\text{GeV}/c^2$ ). Figure 8 shows the two-jet invariant mass distributions for data and the estimated background. The normalization factor is found to be  $N_V = N_{VB}/(N_{\text{cand}} - N_{\text{QCD}}/N_F)$ , where  $N_{VB}(= 879)$ ,  $N_{\text{cand}}(= 392)$ , and  $N_{\text{QCD}}(= 251)$  are the numbers of VECBOS events, candidates, and QCD multijet events outside the  $W$  boson mass window, respectively. We find  $N_V = 3.41 \pm 0.31(\text{stat}) \pm 0.29(\text{syst})$ . Using this normalization factor, we estimate  $279.5 \pm 27.2$  (stat)  $\pm 23.8$  (syst)  $W+ \geq 2$  jets events in the candidate sample. The systematic uncertainty is due to the normalization of the multijet background (6.9%), jet energy scale (4%), and the variation when the  $M_{jj}$  requirement is changed to (40,120) or (60,100)  $\text{GeV}/c^2$  (3%). The cross section times branching ratio for  $W+ \geq 2$  jets production with the  $W$  boson decaying to  $e\nu$  determined with this method is  $38795/(3.4 \times 82.3) = 138.6 \pm 14.3$  pb (where 38795 is the number of VECBOS events generated, 3.4 is the normalization factor  $N_V$ , and 82.3 pb $^{-1}$  is the integrated luminosity of the data sample), which is consistent with the value (135 pb) given by the VECBOS program. Figure 9 shows  $p_T(e\nu) - p_T(jj)$  and  $\Delta\mathcal{R}(jj)$  distributions, which are important measures for how well background estimates describe the jets in the data. The backgrounds include the  $W+ \geq 2$  jets and QCD multijet contributions. The data and the backgrounds agree well.

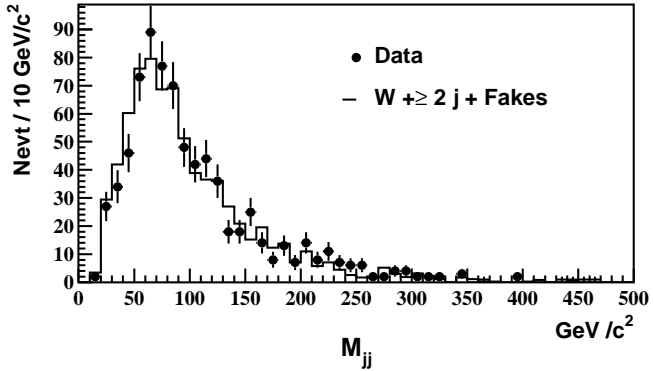


FIG. 8. Dijet invariant mass distribution. The solid circles and the histogram are the candidate events and the background events from  $W+ \geq 2$  jet events plus QCD multijet events with a fake electron, respectively.

## 2. $t\bar{t} \rightarrow W^+W^-b\bar{b} \rightarrow e\nu jjX$

Since no limit on the number of jets is applied to retain high efficiency,  $t\bar{t} \rightarrow W^+W^-b\bar{b} \rightarrow e\nu jjX$  events contribute to the candidate sample. A sample, simulated using **ISAJET** with  $M_t = 170$   $\text{GeV}/c^2$ , is used to estimate this contribution. We find it to be small,  $3.7 \pm 0.3$  (stat)  $\pm 1.3$  (syst) events. The production cross section for  $t\bar{t}$  events is taken from the DØ measurement ( $5.2 \pm 1.8$  pb) [31]. The error in this measurement (35%) is included as a systematic uncertainty in our analysis.

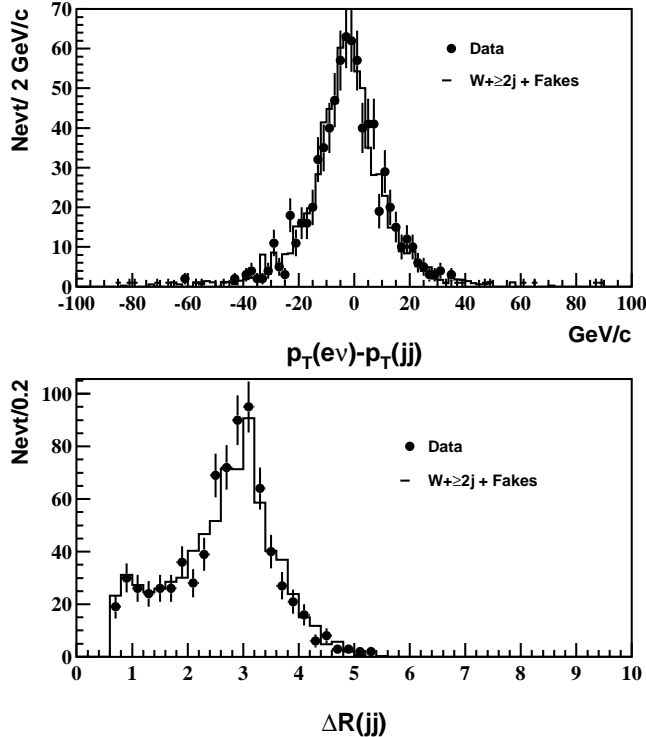


FIG. 9. Upper plot:  $p_T(e\nu) - p_T(jj)$  distribution before mass window requirement. Lower plot:  $\Delta R(jj)$  distribution for the two jets.

### 3. $WW/WZ \rightarrow \tau\nu jj \rightarrow e\nu\nu jj$

Since the contribution from  $WW/WZ \rightarrow \tau\nu jj \rightarrow e\nu\nu jj$  is small, and no separate signal simulation is available, we treat it as background. We use the ISAJET event generator and the detailed detector simulation program to estimate this background. The  $WW$  and  $WZ$  production cross sections are assumed to be 9.5 pb and 2.5 pb, respectively. After event selection, we find  $0.15^{+0.16}_{-0.08}$  (stat)  $\pm 0.01$  (syst) events. The systematic uncertainty on the background estimate is assigned to be the largest value of the asymmetric errors on the theoretical cross section (8.4%) [28].

### 4. $ZX \rightarrow e^+e^-X$

The  $ZX \rightarrow eeX$  processes can produce events which could be misidentified as the signal. These events may be included in the candidate sample if one electron goes through a calorimeter module boundary and is measured as  $E_T$  in the event. From a sample of 10000 ISAJET  $ZX \rightarrow e^+e^-X$  events generated, none of them survive the selection procedure. The background from events of this type is negligible.

### 5. $ZX \rightarrow \tau^+\tau^-X \rightarrow e\nu jjX$

The  $ZX \rightarrow \tau\tau X$  processes can produce events which could fake the signal if, due to statistical fluctuations, one or two jets from ISR or FSR with enough energy are detected. From a sample of 10000 PYTHIA-generated  $ZX \rightarrow \tau\tau X$  events, none survive our selection. The background from this source is negligible.

## IX. RESULTS

After the event selection, 399 candidates remain. The numbers of events expected from SM  $WW/WZ$  processes and the background processes are  $17.5 \pm 3.0$  events and  $387.5 \pm 38.1$  events, respectively. The transverse mass distribution of the candidate events is shown in Fig. 10 along with the major background contributions and the SM production of  $WW/WZ$  events. The distributions for the data and the background agree well. Table IV summarizes the numbers of events for candidates, estimated backgrounds, and SM predictions from the Run 1a and 1b data samples.

TABLE IV. Numbers of events for backgrounds, data and SM prediction for Run 1a and Run 1b samples.

	Run 1a	Run 1b
Luminosity	$13.7 \text{ pb}^{-1}$	$82.3 \text{ pb}^{-1}$
Background		
QCD multijet	$12.2 \pm 2.6$	$104.3 \pm 12.3$
$W + \geq 2$ jets	$62.2 \pm 13.0$	$279.5 \pm 36.0$
$t\bar{t} \rightarrow e\nu jj + X$	$0.87 \pm 0.12$	$3.7 \pm 1.3$
Total background	$75.5 \pm 13.3$	$387.5 \pm 38.1$
Data	84	399
SM $WW+WZ$ prediction	$3.2 \pm 0.6$	$17.5 \pm 3.0$

Figure 11 shows the  $p_T$  distributions of the  $e\nu$  system for data, background estimates, and SM predictions. We do not observe a statistically significant signal above the background.

Among the 399 events that satisfy the selection criteria, 18 events are found with  $p_T(e\nu) > 100 \text{ GeV}/c$ . The numbers of background and SM production events in this  $p_T$  range are estimated to be  $18.5 \pm 1.8$  and  $3.2 \pm 0.5$ , respectively. The absence of an excess of events with high  $p_T(e\nu)$  excludes large deviations from the SM couplings. The data are in good agreement with SM event production.

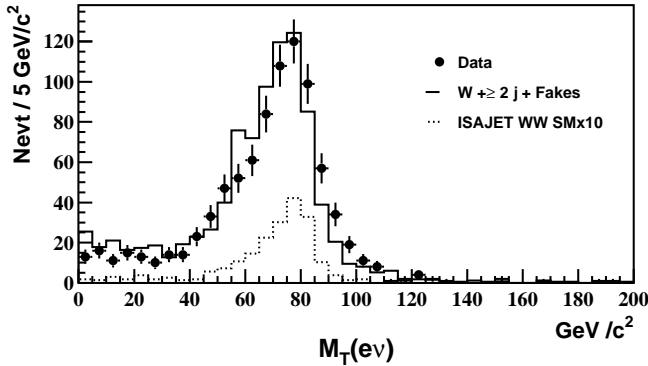


FIG. 10. Transverse mass distributions of the electron and  $\not{E}_T$  system. The solid circles, solid histogram, and dotted histogram are the candidate events, the background from QCD multijet events with a fake electron plus  $W + \geq 2$  jet events, and SM production of  $WW/WZ$  events scaled up by a factor of ten, respectively.

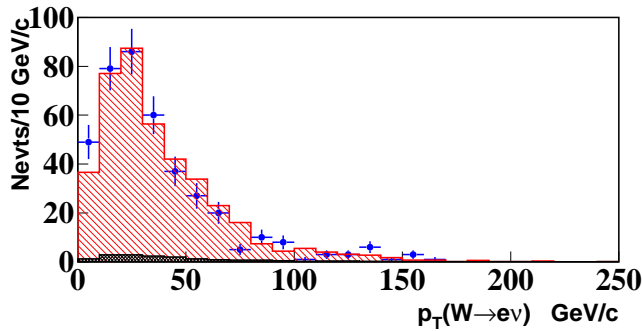


FIG. 11. The  $p_T$  distributions of the  $e\nu$  system from the 1993–1995 (Run 1b) data sample. The solid circles are data with  $1\sigma$  error bars. The light-shaded histogram is the SM prediction plus the background estimates and the dark-shaded histogram is the SM prediction for  $WW/WZ$  processes.

### A. Limits on the Anomalous Couplings Using Minimum $p_T^W$

The  $WW/WZ$  production cross section increases as the coupling parameters deviate from the SM values, especially at high  $p_T^W$ , as shown in Fig. 2. The  $p_T^W$  distribution of background events is softer than that of  $WW/WZ$  production with anomalous couplings. When only events with  $p_T^W$  above a large minimum value are selected, almost all background events are rejected, but a good fraction of signal events with anomalous couplings remains, providing a better sensitivity to anomalous couplings. This method also eliminates SM production events and therefore does not have sensitivity to the SM couplings.

The 95% C.L. upper limit on the number of observed events,  $N^{95\% \text{C.L.}}$ , is obtained from the number of observed candidate events and the estimated background with a minimum  $p_T^W$  requirement.

Monte Carlo events have been generated for pairs of anomalous couplings in grid points of  $\Delta\kappa$  and  $\lambda$ . We assume that the couplings for  $WW\gamma$  and  $WWZ$  are equal in this study.

The expected number of events is calculated for each pair of anomalous couplings using the integrated luminosity of the data sample and is put into a two-dimensional histogram with  $\Delta\kappa$  and  $\lambda$  as coordinate axes. The surface of the histogram is fitted with a two-dimensional parabolic function. Limits on the anomalous couplings at the 95% C.L. are calculated from the intersection of the two-dimensional parabolic surface of the predicted number of events with a plane of  $N^{95\% \text{C.L.}}$ . The resulting contour is an ellipse in the  $\Delta\kappa - \lambda$  plane. The numerical values of the one degree-of-freedom 95% C.L. limits are summarized in Table V for different minimum  $p_T^W$  values.

TABLE V. Limits on  $\lambda$  and  $\Delta\kappa$  at the 95% C.L. as a function of minimum  $p_T^W$  for  $\Lambda = 1.5$  TeV. The numbers of candidates ( $N_{\text{cand}}$ ), background ( $N_{\text{BG}}$ ) estimates, and SM  $WW/WZ$  predictions ( $N_{\text{SM}}$ ) are also shown.

$p_T^W$ (GeV/c)	$N_{\text{cand}}$ events	$N_{\text{BG}}$ events	$N_{\text{SM}}$ events	$\lambda$ ( $\Delta\kappa = 0$ )	$\Delta\kappa$ ( $\lambda = 0$ )
150	4	2.8	1.9	(-0.66, 0.67)	(-0.96, 1.08)
160	1	2.1	1.8	(-0.54, 0.54)	(-0.79, 0.89)
170	0	1.5	0.9	(-0.52, 0.52)	(-0.76, 0.86)
180	0	1.2	0.2	(-0.59, 0.58)	(-0.87, 0.96)
190	0	0.7	0.1	(-0.64, 0.64)	(-0.96, 1.05)
200	0	0.3	0.1	(-0.74, 0.73)	(-1.13, 1.20)

## B. Limits on Anomalous Couplings from the $p_T^W$ Spectrum

The limits obtained with a minimum  $p_T^W$  do not take into account information that may be found in the full  $p_T^W$  spectrum, and depend on the minimum  $p_T$  value as well as the overall normalization factors for background estimates and theoretical predictions of signal. An alternative method is to fit the shape of kinematical distributions which are sensitive to anomalous couplings. This method usually provides tighter limits, since it uses all the information contained in the differential distributions, and it is less sensitive to the overall normalization factors.

As described in Sec. I, the differential distribution which is most sensitive to anomalous couplings is the  $p_T^{W(Z)}$  distribution. This analysis uses the  $p_T(W \rightarrow e\nu)$  spectrum rather than  $p_T(W \rightarrow jj)$  or  $p_T(Z \rightarrow jj)$ . The resolution of  $p_T(e\nu)(12.5 \text{ GeV}/c)$  is better than that of  $p_T(jj)(16.7 \text{ GeV}/c)$ . This is primarily due to the ambiguity in assigning jets to the  $W(Z)$  boson.

The use of the differential cross sections to obtain limits on trilinear gauge boson couplings has been exploited by previous publications [9–11, 13–16, 18, 19]. We use a modified binned  $p_T^W$  fit method to obtain limits. The modification is to add an extra bin with no observed events in the  $p_T^W$  spectrum and improve the sensitivity to anomalous couplings [32].

Based on the distribution of the  $WW/WZ \rightarrow e\nu jj$  events, we choose two 25  $\text{GeV}/c$  bins from 0 to 50  $\text{GeV}/c$ , five 10  $\text{GeV}/c$  bins from 50 to 100  $\text{GeV}/c$ , two 20  $\text{GeV}/c$  bins from 100 to 140  $\text{GeV}/c$ , one 30  $\text{GeV}/c$  bin from 140 to 170  $\text{GeV}/c$  and a single bin above 170  $\text{GeV}/c$  up to 500  $\text{GeV}/c$ . The cross section for  $p_T^W > 500 \text{ GeV}/c$  is negligible for anomalous couplings of any strength allowed by the unitarity constraint. In each  $p_T^W$  bin  $i$ , the probability  $P_i$  for observing  $N_i$  events is given by the Poisson distribution:

$$P_i = \frac{(b_i + \mathcal{L}\epsilon_i\sigma_i(\lambda, \Delta\kappa))^{N_i}}{N_i!} e^{-(b_i + \mathcal{L}\epsilon_i\sigma_i(\lambda, \Delta\kappa))},$$

where  $\mathcal{L}$  is the luminosity, and  $b_i$ ,  $\epsilon_i$ , and  $\sigma_i$  are the expected background, the detection efficiency, and the cross section, respectively, for bin  $i$ . A fast Monte Carlo is used to calculate  $\epsilon_i\sigma_i(\lambda, \Delta\kappa)$ . The joint probability for all  $p_T^W$  bins is the product of the individual probabilities  $P_i$ ,  $P = \prod_{i=1}^{N_{\text{bin}}} P_i$ . Since the values  $\mathcal{L}$ ,  $b_i$ , and  $\epsilon_i$  are measured values with some uncertainty, we assign them Gaussian prior distributions of mean  $\mu = 1$  and standard deviation of  $\sigma_x$ :

$$P' = \int \mathcal{G}_{f_n} df_n \int \mathcal{G}_{f_b} df_b \prod_{i=1}^{N_{\text{bin}}} \frac{e^{f_n n_i + f_b b_i} (f_n n_i + f_b b_i)^{N_i}}{N_i!},$$

where  $n_i = \mathcal{L}\epsilon_i\sigma_i$  is the predicted number of events, and  $\mathcal{G}_{f_n}$  and  $\mathcal{G}_{f_b}$  are Gaussian distributions. The integrals are calculated using 50 evenly spaced points between  $\pm 3\sigma$ . For convenience, the log-likelihood,  $L = \log P'$ , is used. The set of couplings that best describes the data is given by the point in the  $\lambda - \Delta\kappa$  plane that maximizes the likelihood given the above equation.

It is conventional to quote the limits on one coupling when all the others are set to their SM values. These axis limits at the 95% C.L. with the assumption that the  $WW\gamma$  and  $WWZ$  couplings are equal are shown in Table VI. The limits are more stringent than those obtained using minimum  $p_T^W$ .

TABLE VI. Limits on anomalous trilinear gauge boson couplings at the 95% C.L. obtained with the  $p_T^W$  fit from the Run 1b data sample.

Couplings	1.0 TeV	1.5 TeV	2.0 TeV
$\lambda_\gamma = \lambda_Z$	−0.50, 0.53	−0.42, 0.45	−0.39, 0.42
$\Delta\kappa_\gamma = \Delta\kappa_Z$	−0.66, 0.90	−0.56, 0.75	−0.52, 0.70
$\lambda_\gamma$ (HISZ)	−0.50, 0.53	−0.42, 0.45	−0.39, 0.42
$\Delta\kappa_\gamma$ (HISZ)	−0.78, 1.15	−0.68, 0.98	−0.63, 0.91
$\lambda_\gamma$ (SM $WWZ$ )	−1.54, 1.58	−1.53, 1.56	
$\Delta\kappa_\gamma$ (SM $WWZ$ )	−2.03, 2.45	−1.79, 2.12	
$\lambda_Z$ (SM $WW\gamma$ )	−0.58, 0.62	−0.49, 0.51	−0.45, 0.48
$\Delta\kappa_Z$ (SM $WW\gamma$ )	−0.86, 1.12	−0.72, 0.93	−0.67, 0.87

Until now, we have assumed that the couplings  $\Delta\kappa$  and  $\lambda$  for  $WWZ$  and  $WW\gamma$  are equal. However, this is not the only possible relationship between them. Another common

assumption leads to the HISZ relations [33]. These relations specify  $\lambda_Z$ ,  $\kappa_Z$ , and  $g_1^Z$  in terms of the independent variables  $\lambda_\gamma$  and  $\kappa_\gamma$ , thus reducing the number of independent couplings from five to two:  $\Delta\kappa_Z = \frac{1}{2}\Delta\kappa_\gamma(1 - \tan^2\theta_W)$ ,  $\Delta g_1^Z = \frac{1}{2}\Delta\kappa_\gamma/\cos^2\theta_W$ , and  $\lambda_Z = \lambda_\gamma$ . The axis limits at the 95% C.L. with these relations are also shown in Table VI.

Since the  $WWZ$  and  $WW\gamma$  couplings are independent, it is interesting to see the limits on one set of anomalous couplings when the other is set to its SM values. Table VI includes the axis limits at the 95% C.L. for both assumptions: limits on  $\Delta\kappa_\gamma$  and  $\lambda_\gamma$  when SM  $WWZ$  couplings are assumed, and limits on  $\Delta\kappa_Z$  and  $\lambda_Z$  when SM  $WW\gamma$  couplings are assumed. The results indicate that this analysis is more sensitive to  $WWZ$  couplings as expected from the larger overall couplings for  $WWZ$  than  $WW\gamma$  and that it is complementary to the  $W\gamma$  production process which is sensitive to the  $WW\gamma$  couplings only.

### C. Combined Run 1 $WW/WZ \rightarrow e\nu jj$ Results

The limits on anomalous couplings presented in this paper are significantly tighter than those given in our previous publications of this channel based on the Run 1a data sample [11,15]. The primary reason for the tighter limits is the increased statistics for the 1993–1995 (Run 1b) data sample (about a factor of six) in comparison with 1992–1993 (Run 1a) data sample. We can obtain even tighter limits if we combine the Run 1a and 1b results. The analysis based on the Run 1a data sample is described in Refs [11,15]. A summary of the signal and backgrounds for the two analyses [18] is shown in Table IV.

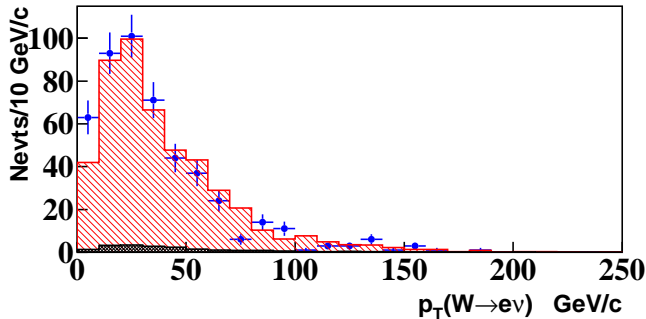
The two analyses can be treated as different experiments. Since both experiments have taken place using the same detector, there are some correlated uncertainties, such as the uncertainties on the luminosity calculation, lepton reconstruction and identification, and the theoretical prediction. Also the background estimate is common to each experiment. The uncertainty on the  $W/Z \rightarrow jj$  selection efficiency is assumed to be uncorrelated, since we use different cone sizes for jet reconstruction in the two analyses. The uncertainties for both analyses are summarized in Tables VII and VIII. Each uncertainty is weighted by the integrated luminosity for the respective data sample. Figure 12 shows the combined  $p_T^W$  spectrum.

TABLE VII. Common systematic uncertainties for Run 1a and Run 1b analyses.

Source of Uncertainty	
Luminosity	5.4%
QCD corrections	14%
Electron and trigger efficiency	1.2%
Statistics of fast MC	1%
$\cancel{E}_T$ smearing	5.1%
Jet energy scale	3.4%
Total	16%

TABLE VIII. Uncorrelated systematic uncertainties for Run 1a and Run 1b analyses.

Source of Uncertainty	Run 1a	Run 1b
ISAJET vs PYTHIA	9%	4%
Stat. uncertainties of $\epsilon(W \rightarrow jj)$	4%	2%
Parametrization of $\epsilon_i \sigma_i(\lambda, \Delta\kappa)$	4%	5%
Total	11%	7%
Background	13%	7%


 FIG. 12. The  $p_T^W$  spectrum for  $e\nu jj$  candidates from the full Run 1 data sample. The solid circles are data with  $1\sigma$  error bars. The light-shaded histogram is the SM prediction plus the background estimates and the dark-shaded histogram is the SM prediction for  $WW/WZ$  processes.

To set limits on anomalous couplings, we combine the results of the two analyses by calculating a combined likelihood function. The individual uncertainties on the signal and backgrounds for each analysis are taken into account as in the previous section. Common systematic uncertainties are taken into account by introducing a common Gaussian prior distribution for the two data samples.

The resulting, combined Run 1a and Run 1b, 95% C.L. contours are shown in Fig. 13. The one and two degree-of-freedom 95% C.L. contour limits (corresponding to log-likelihood function values 1.92 and 3.00 units below the maximum, respectively) are shown as the inner curves, along with the  $S$ -matrix unitarity limits, shown as the outermost curves. Figure 13(a) shows the contour limits when couplings for  $WW\gamma$  are assumed to be equal to those for  $WWZ$ . Figure 13(b) shows contour limits assuming the HISZ relations. In Figs. 13(c) and 13(d), SM  $WW\gamma$  couplings are assumed and the limits for  $WWZ$  couplings are shown. When SM  $WW\gamma$  couplings are assumed, the  $U(1)$  point that corresponds to the condition in which there is no  $WWZ$  couplings ( $\kappa_Z = 0$ ,  $\lambda_Z = 0$ ,  $g_1^Z = 0$ ) is excluded at the 99% C.L. This is direct evidence for the existence of the  $WWZ$  couplings. Limits are slightly improved, compared with the results from the 1993–1995 data sample alone. The 95% C.L. limits on the axes are listed in Table IX for four assumptions on the relation between  $WW\gamma$  and  $WWZ$  couplings: (i)  $\Delta\kappa \equiv \Delta\kappa_\gamma = \Delta\kappa_Z$ ,  $\lambda \equiv \lambda_\gamma = \lambda_Z$ , (ii) HISZ relations, (iii) SM  $WW\gamma$  couplings, and (iv) SM  $WWZ$  couplings.

TABLE IX. Limits on anomalous trilinear gauge boson couplings at 95% C.L. from the combined Run 1a and Run 1b data samples for these values of  $\Lambda$ .

Couplings	1.0 TeV	1.5 TeV	2.0 TeV
$\lambda_\gamma = \lambda_Z$	−0.42, 0.45	−0.36, 0.39	−0.34, 0.36
$\Delta\kappa_\gamma = \Delta\kappa_Z$	−0.55, 0.79	−0.47, 0.63	−0.43, 0.59
$\lambda_\gamma$ (HISZ)	−0.42, 0.45	−0.36, 0.39	−0.34, 0.36
$\Delta\kappa_\gamma$ (HISZ)	−0.69, 1.04	−0.56, 0.85	−0.53, 0.78
$\lambda_\gamma$ (SM $WWZ$ )	−1.28, 1.33	−1.21, 1.25	
$\Delta\kappa_\gamma$ (SM $WWZ$ )	−1.60, 2.03	−1.38, 1.70	
$\lambda_Z$ (SM $WW\gamma$ )	−0.47, 0.51	−0.40, 0.43	−0.37, 0.40
$\Delta\kappa_Z$ (SM $WW\gamma$ )	−0.74, 0.99	−0.60, 0.79	−0.54, 0.72
$\Delta g_1^Z$ (SM $WW\gamma$ )	−0.75, 1.06	−0.64, 0.89	−0.60, 0.81

## X. CONCLUSIONS

A search for anomalous  $WW$  and  $WZ$  production in the  $e\nu jj$  decay mode at  $\sqrt{s} = 1.8$  TeV has been performed. In a total of  $82.3 \text{ pb}^{-1}$  of data from the 1993–1995 collider run at Fermilab, we observe 399 candidate events with an expected background of  $387.5 \pm 38.1$  events. The expected number of events from SM  $WW/WZ$  production is  $17.5 \pm 3.0$  events for this integrated luminosity. The sum of the SM prediction and the background estimates is consistent with the observed number of events, indicating that no new physics phenomena is seen. Comparing the  $p_T^W$  distributions of the observed events with theoretical predictions, we set limits on the  $WW\gamma$  and  $WWZ$  anomalous couplings. The limits on anomalous couplings are significantly tighter than those using the data from the 1992–1993 data sample. The two results are combined to set even tighter limits on the anomalous couplings. With an assumption that the  $WW\gamma$  and  $WWZ$  couplings are equal, we obtain  $-0.34 < \lambda < 0.36$  (with  $\Delta\kappa = 0$ ) and  $-0.43 < \Delta\kappa < 0.59$  (with  $\lambda = 0$ ) at the 95% C.L. for a form factor scale  $\Lambda = 2.0 \text{ TeV}$  [34].

## XI. ACKNOWLEDGEMENTS

We thank the Fermilab and collaborating institution staffs for contributions to this work, and acknowledge support from the Department of Energy and National Science Foundation (USA), Commissariat à L’Energie Atomique (France), Ministry for Science and Technology and Ministry for Atomic Energy (Russia), CAPES and CNPq (Brazil), Departments of Atomic Energy and Science and Education (India), Colciencias (Colombia), CONACYT (Mexico), Ministry of Education and KOSEF (Korea), CONICET and UBACyT (Argentina), A.P. Sloan Foundation, and the Humboldt Foundation.

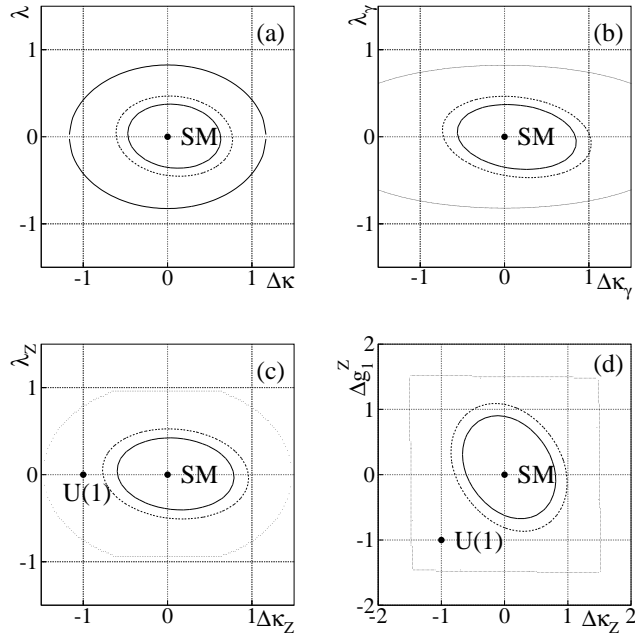


FIG. 13. Contour limits on anomalous couplings at the 95% C.L. (two inner curves) and unitary constraints (outermost curves), assuming (a)  $\Delta\kappa \equiv \Delta\kappa_\gamma = \Delta\kappa_Z$ ,  $\lambda \equiv \lambda_\gamma = \lambda_Z$ ; (b) HISZ relations; (c) and (d) SM  $WW\gamma$  couplings.  $\Lambda = 1.5$  TeV is used for all four cases. The  $U(1)$  point indicates that there are no  $WWZ$  couplings.

## REFERENCES

- [1] U. Baur and E. L. Berger, Phys Rev. D **41**, 1476 (1990).
- [2] K. Hagiwara, J. Woodside and D. Zeppenfeld, Phys Rev. D **41**, 2113 (1990).
- [3] J. Ellison and J. Wudka, UCR-D0-98-01, 1998, hep-ph/9804322 (unpublished).
- [4] Particle Data Group, Eur. Phys. J. C **3**, 1 (1998).
- [5] K. Hagiwara, R.D. Peccei, D. Zeppenfeld and K. Hikasa, Nucl. Phys. **B282**, 253 (1987).
- [6] F. Boudjema *et al.*, Phys. Rev. D **43**, 2223 (1991).
- [7] U. Baur and D. Zeppenfeld, Phys. Lett. B **201**, 383 (1988).
- [8] J. Alitti *et al.* (UA2 Collaboration), Phys. Lett. B **277**, 194 (1992).
- [9] F. Abe *et al.* (CDF Collaboration), Phys. Rev. Lett. **74**, 1936 (1995).
- [10] S. Abachi *et al.* (DØ Collaboration), Phys. Rev. Lett. **75**, 1034 (1995); *ibid.*, **78**, 3634 (1997).
- [11] S. Abachi *et al.* (DØ Collaboration), Phys. Rev. D **56**, 6742 (1997)
- [12] F. Abe *et al.* (CDF Collaboration), Phys. Rev. Lett. **78**, 4536 (1997).
- [13] S. Abachi *et al.* (DØ Collaboration), Phys. Rev. Lett. **75**, 1023 (1995); B. Abbott *et al.* (DØ Collaboration), Phys. Rev. D **58**, 051101 (1998).
- [14] F. Abe *et al.* (CDF Collaboration), Phys. Rev. Lett. **75**, 1017 (1995).
- [15] S. Abachi *et al.* (DØ Collaboration), Phys. Rev. Lett. **77**, 3303 (1996).
- [16] B. Abbott *et al.* (DØ Collaboration), Phys. Rev. D, **60**, 072002 (1999)

[17] P. Abreu *et al.* (DELPHI Collaboration), Phys. Lett. B **459**, 382 (1999); G. Abbiendi *et al.* (OPAL Collaboration), Eur. Phys. J. C **8**, 191 (1999); M. Acciarri *et al.* (L3 Collaboration), CERN-EP-99-131, 1999, submitted to Phys. Lett. B; B. Barate *et al.* (ALEPH Collaboration), CERN-EP-98-178, 1998, submitted to Phys. Lett. B.

[18] B. Abbott *et al.* (DØ Collaboration), Phys. Rev. Lett. **79**, 1441 (1997).

[19] A. Sánchez-Hernández, Ph.D. Dissertation, CINVESTAV, Mexico City, Mexico (1997), [http://www-d0.fnal.gov/results/publications\\_talks/thesis/thesis.html](http://www-d0.fnal.gov/results/publications_talks/thesis/thesis.html), unpublished.

[20] S. Abachi *et al.* (DØ Collaboration), Nucl. Instrum. Methods in Phys. Res. A **338**, 185 (1994).

[21] S. Abachi *et al.* (DØ Collaboration), Phys. Rev. Lett. **77**, 3309 (1996); B. Abbott *et al.* (DØ Collaboration), Phys. Rev. Lett. , **80**, 3008 (1998); Phys. Rev. D **58**, 12002 (1998); *ibid.*, **58**, 092003 (1998); B. Abbott *et al.* (DØ Collaboration), FERMILAB-Pub-99/237-E, hep-ex/9908057 (submitted to Phys. Rev. D); B. Abbott *et al.* (DØ Collaboration), FERMILAB-Pub-99/259-E, hep-ex/9909030 (to appear in Phys. Rev. Lett.).

[22] DØ Collaboration, R. Kehoe, in *Proceedings of the sixth International Conference on Calorimetry in High Energy Physics, Frascati, Italy* (World Scientific, River Edge, NJ, 1996), FERMILAB-Conf-96/284-E.

[23] J. Bantly *et al.*, FERMILAB-TM-1995 (unpublished). In order to facilitate combination with previously published results, this analysis does not use the luminosity normalization given in B. Abbott *et al.* (DØ Collaboration), hep-ex/990625, sec. VII, pp. 21-22 (submitted to Phys. Rev. D). The updated normalization would have the effect of increasing the luminosity by 3.2%.

[24] M. L. Kelly, Ph.D. Thesis, Notre Dame (1996), [http://www-d0.fnal.gov/results/publications\\_talks/thesis/thesis.html](http://www-d0.fnal.gov/results/publications_talks/thesis/thesis.html), unpublished.

[25] F. Paige and S. Protopopescu, BNL Report BNL38034 (1986), unpublished. We used version 7.22.

[26] T. Sjöstrand, Comput. Phys. Commun. **82**, 74 (1994).

[27] H. L. Lai *et al.* Phys. Rev. D **51**, 4763 (1995).

[28] J. Ohnemus, Phys. Rev. D **44**, 1403 (1991); *ibid.*, **44**, 3477 (1991).

[29] F.A. Berends *et al.*, Nucl. Phys. **B357**, 32 (1991). We used version 3.0.

[30] G. Marchesini *et al.*, Comput. Phys. Commun. **67**, 465 (1992). We used version 5.7.

[31] B. Abbott *et al.* (DØ Collaboration), Phys. Rev. Lett. **79**, 1203 (1997).

[32] G. L. Landsberg, Ph.D. Thesis, State University of New York at Stony Brook (1994), [http://www-d0.fnal.gov/results/publications\\_talks/thesis/thesis.html](http://www-d0.fnal.gov/results/publications_talks/thesis/thesis.html), unpublished.

[33] K. Hagiwara, S. Ishihara, R. Szalapski and D. Zeppenfeld, Phys. Rev. D **48**, 2182 (1993); Phys. Lett. B **283**, 353 (1992). They parametrize the  $WWZ$  couplings in terms of the  $WW\gamma$  couplings:  $\Delta\kappa_Z = \Delta\kappa_\gamma(1 - \tan^2\theta_W)/2$ ,  $\Delta g_1^Z = \Delta\kappa_\gamma/2\cos^2\theta_W$  and  $\lambda_Z = \lambda_\gamma$ .

[34] Subsequent to the publication of Ref. [18] which summarized this analysis, these results were combined with the other DØ measurements of anomalous  $WW\gamma$  and  $WWZ$  couplings, using the method described in B. Abbott *et al.* (DØ Collaboration), Phys. Rev. D **58** 31102 (1998), to provide the experiment's most restrictive limits reported in

Ref. [16].